



## Research on precision inspection of subsea pipeline defects based on dry cabin and structured light

Hai Zhu<sup>a</sup>, Yuan Lin<sup>a</sup>, Zhangyong Jin<sup>a</sup>, Jin Guo<sup>a</sup>, Peiwen Lin<sup>a</sup>, Jiawang Chen<sup>a,b,\*</sup>, Jie Chen<sup>c</sup>, Han Ge<sup>a</sup>, Kaichuang Wang<sup>a</sup>, Haonan Li<sup>a</sup>, Xiaoqing Peng<sup>a</sup>, Peng Zhou<sup>a</sup>, Yuping Fang<sup>a</sup>, Xueyu Ren<sup>a</sup>, Yuhong Wang<sup>a</sup>, Yongqiang Ge<sup>a</sup>, Xu Gao<sup>a,d</sup>, Yuanjie Chen<sup>c</sup>

<sup>a</sup> Institute of Ocean Engineering and Technology, Zhejiang University, Zhoushan, Zhejiang 316021, China

<sup>b</sup> Donghai Laboratory, Zhoushan, Zhejiang 316021, China

<sup>c</sup> Zhejiang Institute of Metrology, Hangzhou, Zhejiang 310063, China

<sup>d</sup> PipeChina Eastern Oil Storage and Transportation Co. Ltd., ZhouXu, Jiangsu 221008, China

### ARTICLE INFO

#### Keywords:

Subsea pipeline  
Precise defect inspection  
Dry cabin  
Structured light  
Point cloud data

### ABSTRACT

Subsea pipelines are critical for offshore oil and gas transportation, but they can suffer from deformation defects caused by various marine factors, which pose significant risks to their safety and integrity. Traditional acoustic and electromagnetic detection methods often fail to accurately scan for defects, especially in challenging sea conditions with high turbidity. This research focuses on the design and validation of the dry cabin medium displacement system (MDS) and structured light scanning system (SLSS) through sea trials. These technologies enable precise inspection of subsea pipeline defects. By processing the obtained editable point cloud data, the dimensional parameters of the underwater pipelines are determined, which can be used to evaluate the severity of damage and risk coefficients. This information facilitates the formulation of targeted repair strategies. Consequently, this study represents an advancement in subsea pipeline defect inspection technologies, providing a more comprehensive approach to assessing and mitigating risks in offshore operations.

### 1. Introduction

The ocean is commonly referred to as the “blue frontier” [1] due to its abundance of resources, which include, but are not limited to, minerals, biological organisms, and water resources. Energy minerals, such as oil, gas, and gas hydrates, are particularly important in subsea formations [2]. The conventional approach for exploiting offshore oil and gas resources involves drilling platforms extracting oil and gas from subsea formations and using subsea pipelines to transport the resources to land-based refineries.

Subsea pipelines trace their origin to the Gulf of Mexico [3], where the world’s first subsea pipeline was constructed in 1954. The Chinese inaugural subsea pipeline was successfully laid out in Huangdao, Shandong, in 1973. With the development of national industrialization, the demand for oil and gas transportation has further expanded, and remarkable strides in national construction capabilities have provided practical underpinnings for cross-sea subsea pipelines. The length of subsea pipelines has experienced phenomenal growth, endowing

offshore oil and gas exploitation with robust capacity. However, the concomitant expansion of subsea pipeline installations has also escalated maintenance difficulties, risk factors, and costs.

Subsea pipelines are a vital lifeline for offshore oil-gas fields [4,5], playing a crucial role in their development, production, and transportation. On the one hand, severe damage or leakage of subsea pipelines can disrupt energy supplies, causing significant economic losses to companies and countries. On the other hand, damage and leakage can also result in severe pollution in the surrounding marine environment, leading to ecological disasters. To ensure the safety of subsea pipelines in different application scenarios, the structural design of subsea pipelines has become increasingly complex and specialized over the past few decades, with various types such as single-layer steel pipe, double-layer insulated steel pipe, internally clad alloy steel pipe, flexible pipe, and bundled pipeline [6–8]. The evolution of structural forms of subsea pipelines reflects that the marine environment destroys the pipeline in a wide range of forms (including corrosion [9–11], reciprocating current scouring [12,13], seabed liquefaction [14], anchorage operation, etc.)

\* Corresponding author at: 101 Haigong Building, Zhoushan Campus, Zhejiang University, Dinghai District, Zhoushan City, Zhejiang Province, China.  
E-mail address: [arwang@zju.edu.cn](mailto:arwang@zju.edu.cn) (J. Chen).

and induces each other. Cross-aggravation occurs from time to time. Some particular reasons will also cause the destruction of subsea pipelines (the Nord Stream Subsea Pipelines [15]), which will have a far-reaching impact on social production, human livelihoods, and the ecological environment.

The demand for accurately identifying the location and extent of damage in subsea pipeline systems has increased in recent years, leading to a consensus within the industry to develop defect inspection technology for subsea pipelines. This development has primarily branched into two directions: internal inspection and external inspection. Currently, subsea pipeline internal inspection is the predominant technology employed due to its diverse technical forms, convenient scanning and scanning capabilities, and relatively low cost [16]. However, the unique requirements of subsea pipelines necessitate inspection equipment that should be highly passability because the repair costs associated with blockages can be prohibitively high. Furthermore, subsea pipeline internal inspection suffers from limitations such as poor positioning accuracy, challenging speed control, and inadequate data point resolution, which constrains its utility. Consequently, developing subsea pipeline external inspection technology represents an important supplement to existing subsea pipeline defect inspection technology.

Subsea pipeline external inspection technologies can generally be classified into geophysical exploration and diving inspection methods. The former includes the use of equipment and techniques such as sub-bottom profilers (SBP), multibeam systems (MBS), side-scan sonar systems (SSS), and magnetic anomaly detectors (MAD) for conventional external inspection of subsea pipelines [17–19]. The latter involves subsea inspections carried out by divers or remotely operated vehicles (ROVs), with primary methods including subsea visual inspections (UWVI), contact point inspections(CPI) [20], ultrasonic testing (UT) [21], eddy current testing (ECT) [22], magnetic flux leakage (MFL) [23], alternating current field measurement (ACFM), and radiographic inspections (RT) [24]. However, When used in isolation, the current state-of-the-art technology of acoustic and electromagnetic detection methods fails to adequately fulfill the demand for quantitatively characterizing defects, providing high scanning precision, facilitating ease of transportation, and operating under harsh sea conditions in subsea pipelines. While optical detection methods offer superior solutions to these issues [25–32], their applicability is often restricted by the peculiarities of the seabed environment, notably, the interference from seawater.

After a thorough investigation, this study has revealed that conventional pipeline inspection methods are incapable of generating comprehensive and accurate 3D models of subsea pipelines, mainly due to two primary obstacles: the hindrance caused by highly turbid seawater and the requirement for exceptional precision. To address these challenges, we have adopted a fresh approach by targeting dry cabins designed for subsea use, which can enable high-precision scanning equipment that was not initially intended for subsea applications. Our research has shown that in China, only one dry cabin is available for non-submerged pipeline repairs [33], and there are no documented instances of dry scanning cabins for pipelines at depths exceeding 30 m. The technical details of the Deepwater Pipeline Repair System (DPRS) developed by DCN in the Netherlands are not publicly accessible. It lacks scanning capabilities, necessitating personnel to work in a high-pressure airlock. In 2008, An underwater habitat clamp (UHC) was presented by Ashbritt, Inc., Enbridge (US), Inc., and Veolia ES, Special Services, Inc. for multi-parameter underwater pipeline repair, which enables repairs on pipelines 6" to 36" in diameter and to depths of up to 33', under one atmosphere of pressure or in a true hyperbaric environment [34]. Nautilus is the world's first subsea pipeline repair robot, which was developed by ARV and Kongsberg Ferrotech. It saves pipeline spot repair operating costs by innovatively completing subsea pipeline maintenance tasks twice as fast as conventional saturation divers' repairs without compromising safety and quality. The Nautilus utilizes an open half-cabin for repairing pipelines but does not include scanning capabilities [35]. Although neither of these overseas devices has scanning

capabilities, they have successfully formed dry cabins subsea, inspiring our research.

## 2. Methodology

### 2.1. Overall structure design

The target of the inspection device at hand is the subsea pipelines connecting Zhoushan and Ningbo, which have been designed to withstand various environmental factors before laying. The pipeline is coated with a concrete weight coating, an epoxy layer, and a Bellota anti-corrosion layer to ensure sufficient anti-corrosion ability and structural strength. Despite these measures, the pipeline has suffered partial joint damage over several years. In 2017, The first party conducted an internal inspection using existing technologies. They identified severe deformation in the pipeline at some points. However, the lack of measurement accuracy prevented the development of corresponding repair plans. Given the parameters of subsea pipeline defects, the inspection device adopted must satisfy the following requirements:

1. The measured length of the pipeline must be  $\geq 5$  m.
2. The measurement accuracy must be  $\leq 1$  mm.
3. Maximum applicable water depth: 30 m.
4. It must be suitable for subsea pipelines with a diameter of 762 mm and capable of forming adaptive seals for pipelines with bending angles of up to 15 degrees.
5. It must be able to produce a 3D editable data model within 6 h.
6. The resulting 3D data model must be highly accurate and editable.

All data must adhere to relevant standards and requirements, ensuring the accuracy and reliability of the scanning results.

The conventional pipeline detection technology struggles to achieve high mapping accuracy in the highly turbid waters of Zhoushan due to the limited precision offered by acoustic and electromagnetic detection methods. While optical methods offer higher precision, they cannot overcome the interference caused by turbid seawater. As a result, we are considering a subsea dry cabin to circumvent the seawater. Structured light mapping technology has extensive applications in areas such as cultural relic restoration and reverse engineering [36–39]. However, there have not been any in-situ subsea pipeline inspection cases. The main challenges in application lie in the waterproofing of the scanner, power supply, remote interface transmission, and motion control. Specifically, for the external mapping of pipeline defects, how to scan large deformation subsea pipelines to achieve full surface coverage is the primary scientific problem that needs to be considered.

The configuration of the subsea pipeline defect mapping device, depicted in Fig. 1, deviates from conventional technical approaches by establishing mapping conditions for subsea structural defect detection using a dry cabin. The integration of structured light technology significantly enhances mapping precision (up to 0.1 mm). The core structure of the mapping device comprises a dry cabin, characterized by a regular hexagonal cross-sectional shape, considering factors such as upstream face dimensions, flow resistance coefficient, internal wiring installation, cabin volume, and opening/closing mechanisms. Supplementary components crucial for functionality include hydraulic winches, adjustable buoyancy chamber, outer frame structure, hydraulic cylinders, counterweights, one-way valves, three-way valve, pneumatic diaphragm pumps, etc., positioned as indicated in Fig. 1. Additionally, non-core structures and equipment encompass high-pressure air ports, liquid level sensors, lifting lugs, drainage pipelines, valves, steel wire ropes, etc., although these are not detailed herein.

As indicated in Fig. 2, trenchers are specialized machines designed to excavate and remove the sediment covering subsea pipelines. They employ rotating cutting blades or water jets to break up the compacted soil above the pipelines, followed by suction systems that lift the loosened material away. This process efficiently exposes buried pipelines

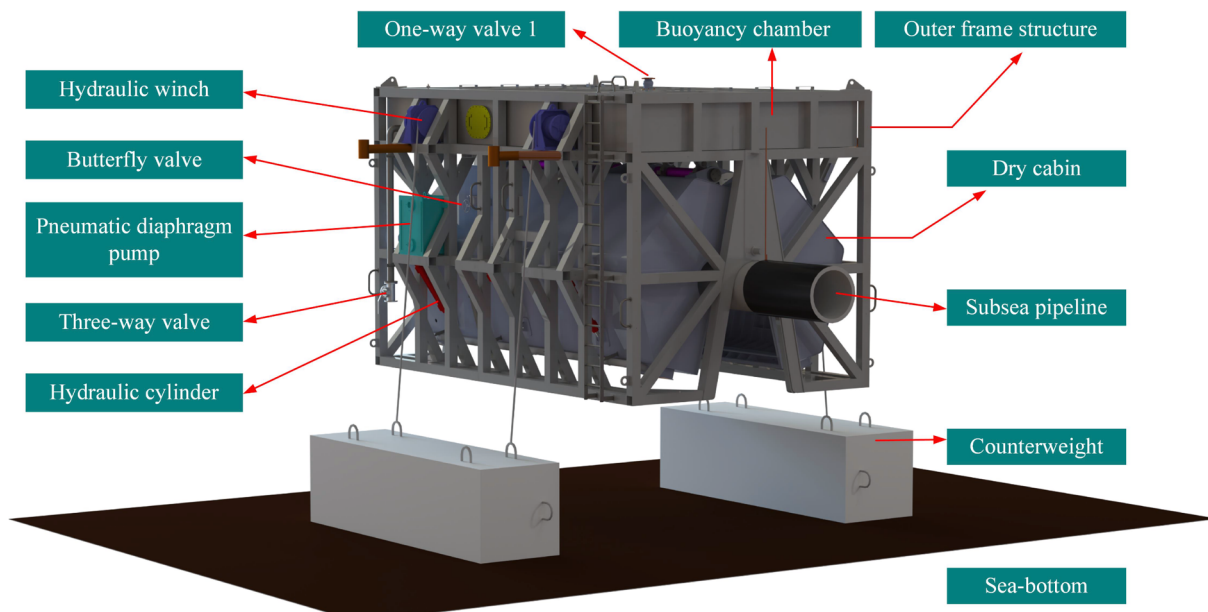


**Fig. 1.** Overall structure of subsea pipeline mapping device.



COOEC' trencher

SMD QT 2800

**Fig. 2.** Trenchers used to clean the soil around the subsea pipeline.

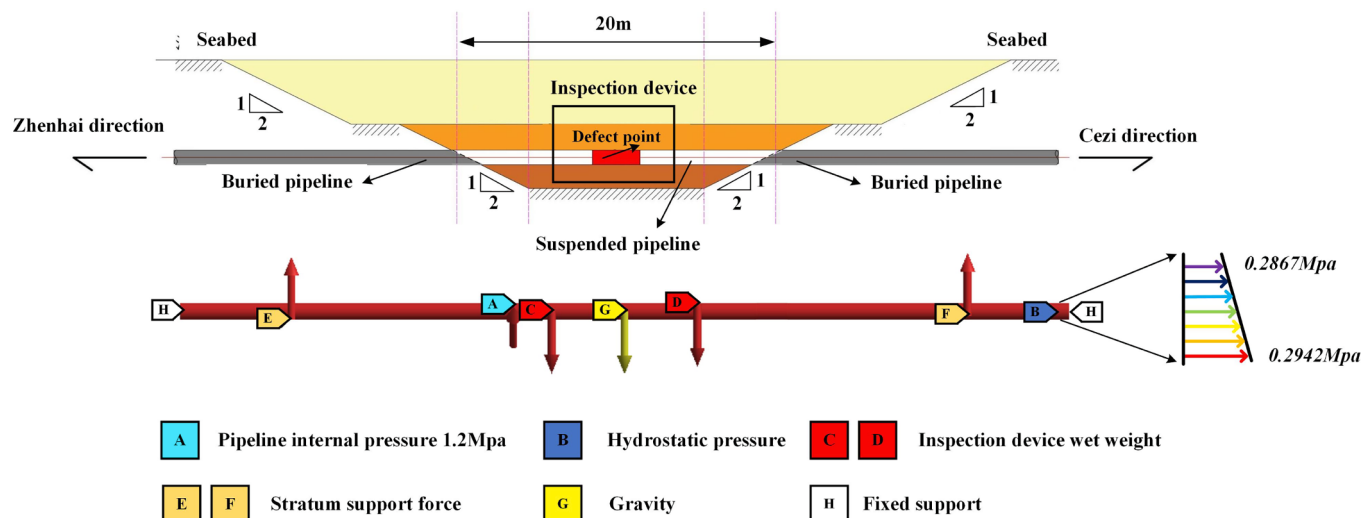


**Fig. 3.** Schematic diagram and force analysis of pipeline crossing operation.

without causing damage, enabling clear access for subsequent inspection and maintenance.

## 2.2. Safety verification

The inspection and maintenance of subsea pipelines rely on trench excavation operations. Consequently, the surveying equipment is deployed across the seabed pipelines. Ensuring the safe operation of the inspection device is crucial due to its substantial weight. According to the "SYT 7056–2016 Subsea Pipelines Free Spanning" standard, as long as the ratio of excavation length to outer diameter ( $L/D$ ) is less than 30, there should be no occurrence of flow-induced and cross-flow-induced vortex-induced vibrations.

**Fig. 3** illustrates an excavation length ( $L$ ) of 20 m for the subsea pipeline, with a diameter of 762 mm. Hence, several factors need to be considered, including internal pressure, hydrostatic pressure, the weight of the inspection device, geological support force, and the pipeline's gravity.

Based on the actual subsea trenching situation, an ANSYS simulation was conducted with certain idealizations. For example, fixed constraints were applied to both ends of the pipeline, considering a strata support length of 10 m on one side of the suspended pipeline. The applied forces, pressures, and dimensional parameters for the simulation are shown in **Table 1**.

The obtained strength and deformation results are shown in **Fig. 4**, respectively. It can be observed that the maximum pressure point is located at the geometric center of the suspended pipeline, with a maximum pressure of 43.757 MPa. The minimum pressure point is situated in the buried section, between the fixed support point and the edge of the suspension, but closer to the fixed support point. The minimum pressure is measured as 0.9511 MPa. These results are consistent with calculations based on material mechanics. The maximum deformation point is also located at the junction of the suspended pipeline, with a maximum deformation of 22.488 mm. This level of deformation is acceptable for a suspension length of 20 m.

Assuming  $G'$  is the self-weight of the inspection device,  $G$  is the self-weight of the pipeline, and the bearing capacity of the foundation per meter is  $f$ , the following expression can be derived:

$$M = \begin{cases} -0.5fx^2 & 0 \leq x \leq 5 \\ 5f(2.5 - x) & 5 < x < 11.739 \\ 12.5f - 5fx + G'(x - 11.739)/2 & 11.739 \leq x \leq 15 \end{cases} \quad (1)$$

Given that the maximum self-weight  $G$  is 94,465 N and  $G'$  is 117,680 N, these values can be converted into the foundation's load-bearing capacity  $f$ . Then:

$$M = \begin{cases} -0.5fx^2 & 0 \leq x \leq 5 \\ 5f(2.5 - x) & 5 < x < 11.739 \\ -2.226421fx - 20.059f & 11.739 \leq x \leq 15 \end{cases} \quad (2)$$

The relationship between bending moment and curvature is used to derive the curvature profile through double integration, resulting in the maximum deformation occurring at the center of the pipeline. For a span of 20 m, the calculated maximum displacement is 24.52 mm. This shows approximately a 9 % discrepancy compared to the 22.488 mm obtained

from simulations.

$$M = EI \frac{d^2y}{dx^2} \quad (3)$$

According to the relationship between stress and bending moment:

$$\sigma = \frac{Mc}{I} \quad (4)$$

in this context,  $c$  represents the distance from the neutral axis to the point where the stress is being calculated, and  $I$  denotes the moment of inertia of the beam's cross-section about the neutral axis. The calculations yield a maximum stress of 42.65 MPa and a minimal stress of 0.945 MPa. These results differ by 2.6 % and 0.65 %, respectively, from those obtained via simulations.

## 2.3. Establishment of subsea dry cabin

The key to the formation of the dry cabin lies in the ability of its seal to form and maintain stability over the long term, making the design of the dry cabin seal structure paramount. To minimize diver intervention and thereby enhance operational efficiency, the seal form and structure necessitate simplicity and effectiveness. To facilitate the wrapping and detachment of the pipeline, it is designed as two semi-cabins that close and dock to achieve sealing. The opening and closing of the dry cabin are executed by hydraulic cylinders and remotely controlled by onboard personnel. The seal structure is simplified by embedding the sealing rubber into U-shaped steel grooves, facilitating the replacement of the sealing rubber.

While using hard rubber for sealing is a common technique, its limited adjustability range leaves little room for adaptation to the uneven surfaces of subsea pipelines and the dry cabin. Therefore, foam sealing rubber is employed at the ends of the dry cabin. As depicted in **Fig. 5**, the end structure is complex, particularly involving the annular sealing surface with the pipeline. Hence, the sealing strip is processed and assembled in segments. The challenge of sealing the upper and lower surfaces of the dry cabin lies in the differing sealing strokes before and after cabin closure. The upper seal stroke is short and does not require adaptive sealing with defect structures, thus hard rubber is used. Conversely, the lower seal stroke necessitates adaptability and utilizes foam rubber.

As shown in **Fig. 6**, the primary methodology employed by MDS to establish a dry cabin entails the utilization of a pneumatic blowing subsystem (PBS) in conjunction with pumps for water drainage. The PBS, employing an air compressor as its air source, operates in tandem with pipelines and valves to effectuate high-pressure air blowing for seawater expulsion within the dry cabin. Traditionally employed in submarines, the PBS functions by gradually introducing high-pressure gas into the dry cabin, thereby increasing internal pressure to balance with external water pressure, and expelling water to the buoyancy chamber until the dry cabin is devoid of water. The depth of the surrounding water determines the hyperbaric gas pressure within the dry cabin, necessitating a specific pressure differential to ensure an effective seal between the cabin and seawater.

Due to the diminished efficacy of high-pressure air blowing in later stages, submersible pumps are employed for seawater suction to enhance displacement efficiency and establish a successful dry environment. Complementarily, two pneumatic diaphragm pumps are utilized to supplement and substitute the submersible pump when it operates without submersion. The buoyancy chamber design accommodates a portion of transferred cabin water, mitigating buoyancy values generated by drainage. Furthermore, to constrain the buoyancy effects on subsea pipelines post-drainage, a hydraulic winch is engaged to tension the steel wire rope connecting the outer frame structure with counterweights, thereby achieving suspension of the entire device and minimizing its impact on seabed pipelines. The values of the PBS-related

**Table 1**  
The applied forces, pressures, and dimensional parameters of safety verification.

Properties	Units	Values	Properties	Units	Values
Strata support length of one side	m	10	Excavation length	m	20
Distance between C → D	mm	6522	Internal pressure of the pipeline	MPa	1.2
Max hydrostatic pressure	MPa	0.2942	Min hydrostatic pressure	MPa	0.2867
The weight of the inspection device	N	117680	Geological support force	N	121457

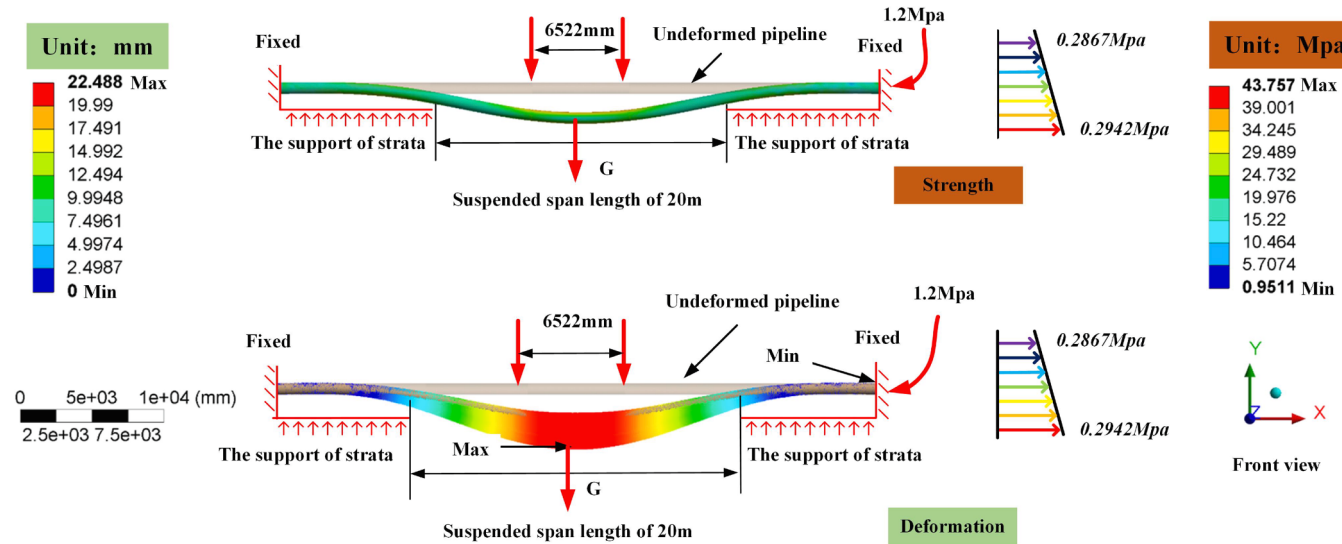


Fig. 4. Strength and deformation simulation results of submarine pipelines.

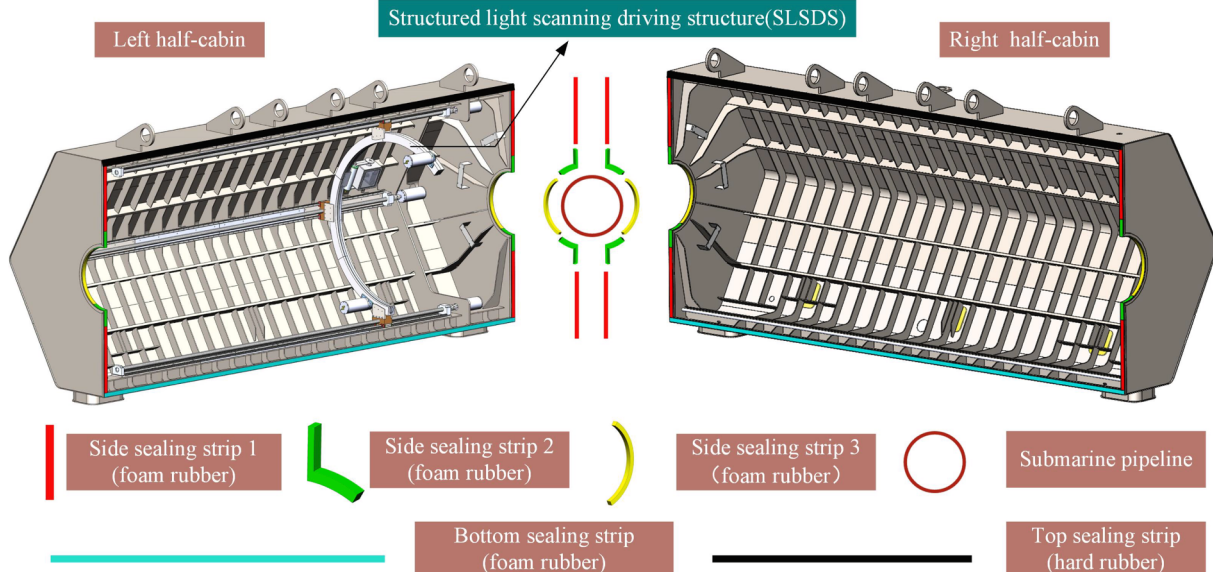


Fig. 5. Overall structure of subsea pipeline mapping device.

parameters in this device are shown in Table 2. The specifications and descriptions for the air compressor, diving pump, and pneumatic diaphragm pumps are detailed in Table 2 of another article we have published [40].

Due to the dry cabin operation basis of the mapping device, both the formation of the dry cabin and the discharge of water from the submarine's ballast tanks rely on hyperbaric gas inflation. Consequently, establishing a theoretical framework for hyperbaric gas inflation becomes particularly necessary, as it is crucial for optimizing and controlling the inflation process. Assuming that the outlet part of the air compressor is section 1, and its air supply pressure is  $p_1$ . The head height is  $Z_1$ . Gas outflow velocity is  $w_1$ . Assume that the entrance of the dry cabin is section 2. The air pressure in the dry cabin is  $p_2$ . The head height is  $Z_2$ . Gas outflow velocity is  $w_2$ . According to Bernoulli's equation:

$$Z_1 + \frac{p_1}{\gamma} + \frac{\alpha w_1^2}{2g} = Z_2 + \frac{p_2}{\gamma} + \frac{\alpha w_2^2}{2g} + h_w + \frac{1}{g} \int_{s_1}^{s_2} \frac{\partial w}{\partial t} ds \quad (5)$$

where  $h_w$  is pipe loss,  $\frac{1}{g} \int_{s_1}^{s_2} \frac{\partial w}{\partial t} ds$  is the inertial head. In the application of

this project, the ratio of the gas supply pipe's sectional area to the tank's sectional area is far less than 0.1, so this item can be ignored. Then we can get:

$$h_w = (Z_1 - Z_2) + \frac{(p_1 - p_2)}{\gamma} + \frac{\alpha(w_1^2 - w_2^2)}{2g} \quad (6)$$

According to the Darcy–Weisbach equation, the calculation formula for pipeline loss  $h_w$  as follows:

$$h_w = h_f + h_j = \sum_{i=1}^n \lambda_i \frac{l_i}{d_i} \frac{w_i^2}{2g} + \sum_{i=1}^n \xi_i \frac{w_i^2}{2g} = w_1^2 \cdot LmdKs \quad (7)$$

Then:

$$Q_1 = A_1 W_1 = A_1 \sqrt{\frac{h_w}{LmdKs}} \quad (8)$$

When the pressure in the tank forces the seawater to flow out of the drain hole, the flow coefficient is assumed to be  $\mu$ , The sectional area of the orifice is  $S$ , and the equivalent head is  $H_0$ , then the outlet flow  $Q_p$  is:

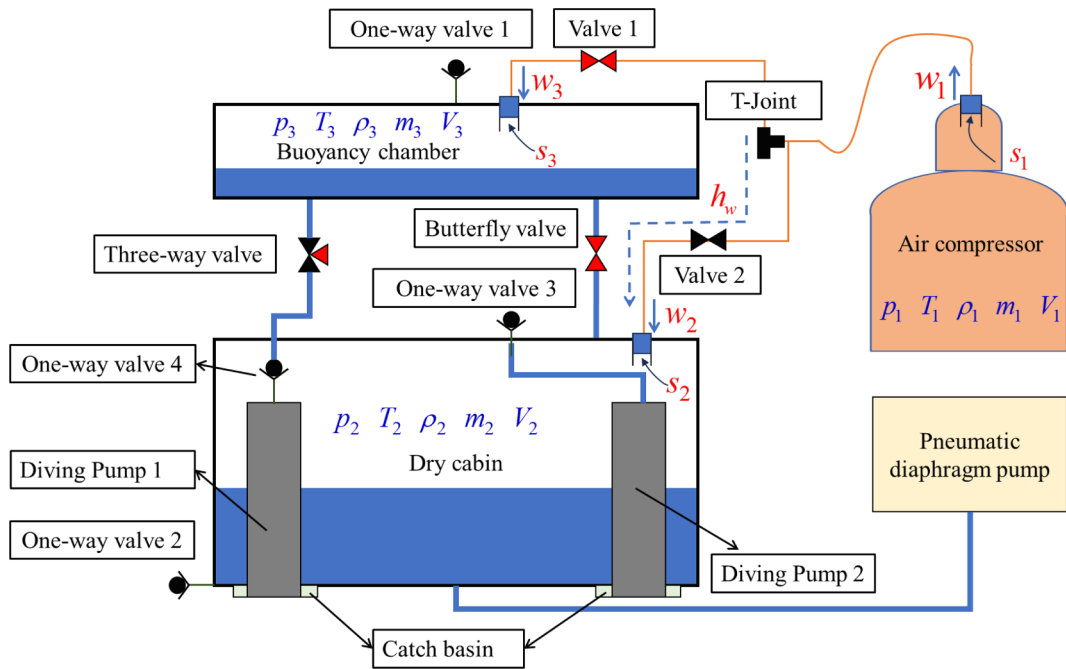


**Fig. 6.** Schematic diagram of medium displacement system [40].

**Table 2**

The PBS-related parameters in this device.

Parameter	Value	Parameter	Value
$S$	7854 mm <sup>2</sup>	$H_0$	44.58 m
$\mu$	0.85	$H - h + h'$	1.2 m
$H_0$	287 mm	$(P_2 - P)/\rho_0 g$	3.3 m
$A_1$	804.25 mm <sup>2</sup>	$V_0^2/2g$	40.08 m
$Q_p$	1.184 m <sup>3</sup> /min	$T$	38 min

$$Q_p = \mu S \sqrt{2gH} \quad (9)$$

Assuming the distance from the orifice to the liquid level is  $h'$ , the distance from the orifice to the dry tank bottom is  $h$ , the atmospheric pressure is  $P$ , the distance from the dry tank bottom to the sea water level is  $H$ , and the internal pressure of the dry tank is  $P_2$ . The falling speed of the water surface is  $V_0$ . Sea water density is  $\rho_0$ , then the equivalent head  $H_0$  is:

$$H_0 = H - h + h' + \frac{P_2 - P}{\rho_0 g} + \frac{V_0^2}{2g} \quad (10)$$

According to the continuous equation of fluid motion  $Q_1 = Q_p$ , the supply pressure and flow rate can be calculated, and the time required to discharge the subsea dry cabin under the supply pressure and flow rate can be calculated.

#### 2.4. Structured light scanning system(SLSS)

The subsea pipeline defect inspection based on the dry cabin is mainly achieved through SLSS, which consists of two main components: the structured light scanning driving structure (SLSDS) and the shipboard electrical control system. As shown in Fig. 7, the SLSDS consists of motors, scanners, seal chambers, circular orbit, slide rails, and so on. After the establishment of the dry cabin, the SLSDS drives a structured light scanner (SLS) to perform a 360° scan around the pipeline while ensuring axial motion within a 5 m range, which is pre-designed and equipped inside the dry cabin. The position change of the scanner is achieved by three drive modules(straight-rail drive module, ring-track drive module, and angle drive module), which cooperate with the

gears to achieve three fundamental functions: axial linear motion, circumferential rotational motion, and small angle adjustment motion. The equipment designed in this study can be used for subsea pipelines with a maximum diameter of 762 mm and a maximum bend angle of 15°, with minimal interference from sea conditions.

The SLS used in this study utilized the principle of triangulation for mapping. As illustrated in Fig. 8, in structured light triangulation, a laser emits a beam of light onto the surface of the object being measured, causing diffuse reflection. A portion of the reflected light is then converged by an imaging system at another angle, forming an image of the light spot on the built-in camera's photosensitive surface. A triangle is formed by the laser, the light spot, and the camera. The distance between the laser and the camera is precisely known, and the angle  $k$  between the light rays diffusely reflected to the camera and the laser emission line is also measurable by the system. Additionally, the angle  $\phi$  between the camera's field of view (FOV) axis and the x-axis, as well as the angle  $d\phi$  between the FOV axis and the laser reflected line, are known. Therefore, the angle between the reflected light ray and the y-axis, representing another internal angle of the triangle, can be determined. Consequently, the distance from the light spot to the scanner can be obtained.

$$d = \frac{l}{\sin k} \sin\left(\frac{\pi}{2} - \phi + d\phi\right) \cos\left(\frac{\pi}{2} + \phi - d\phi - k\right) \quad (11)$$

According to the scanner's perspective and the requirement for the coverage rate of adjacent scans to be greater than 1/3, linear scanning and circular scanning methods are designed based on the size of the annular track. The linear scanning process, as shown on the left side of Fig. 9, involves first obtaining a single scan segment by moving straight, followed by clockwise rotation of 35° and counterclockwise rotation of 15° to enhance stitching success and ensure overlap to avoid data loss. Subsequently, the process repeats to acquire the second scan segment, and this cycle continues until 360° coverage of the pipeline surface is achieved. In contrast, circular scanning begins with circular scanning, followed by linear movement for the next circular scan, and this process repeats until full coverage scanning of the pipeline is completed, which is shown in Fig. 8.

The propulsion system of the motor relies on the shipboard electrical control system. Its fundamental principle involves utilizing an upper

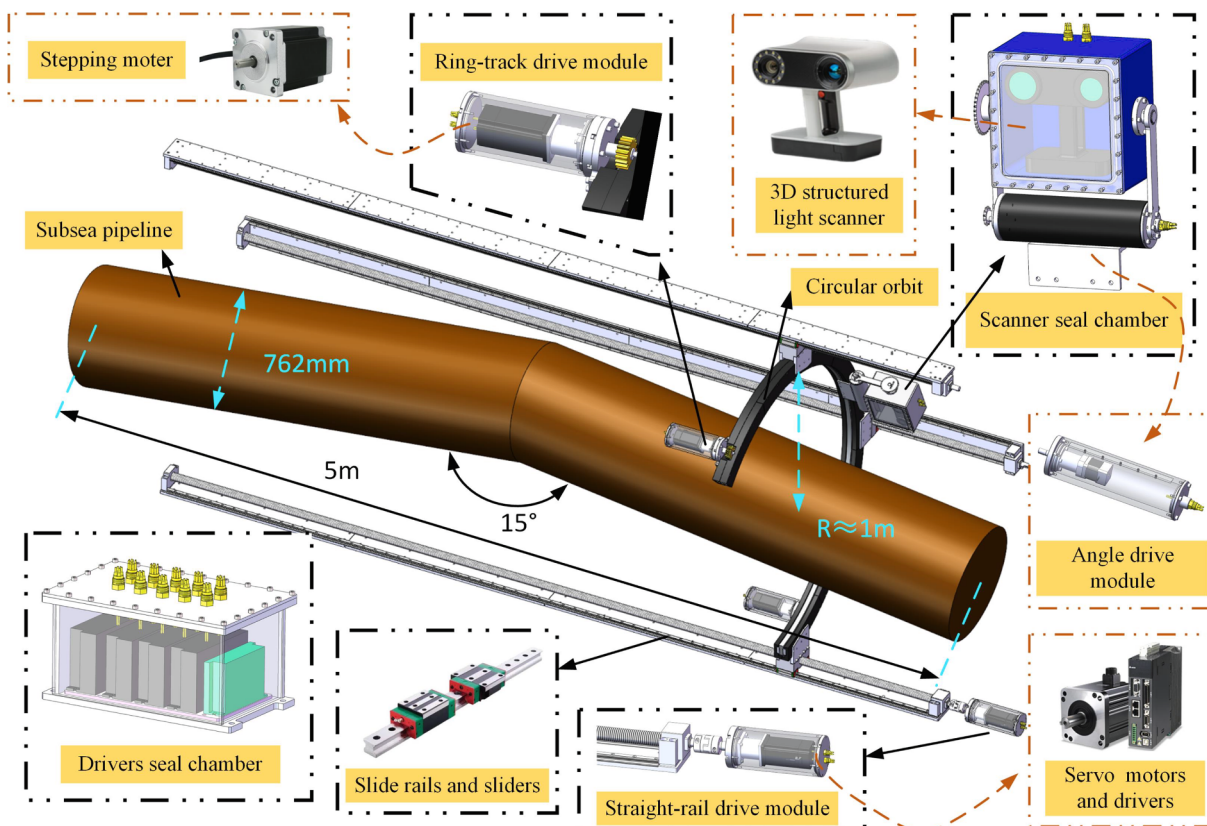


Fig. 7. Structured light scanning driving structure.

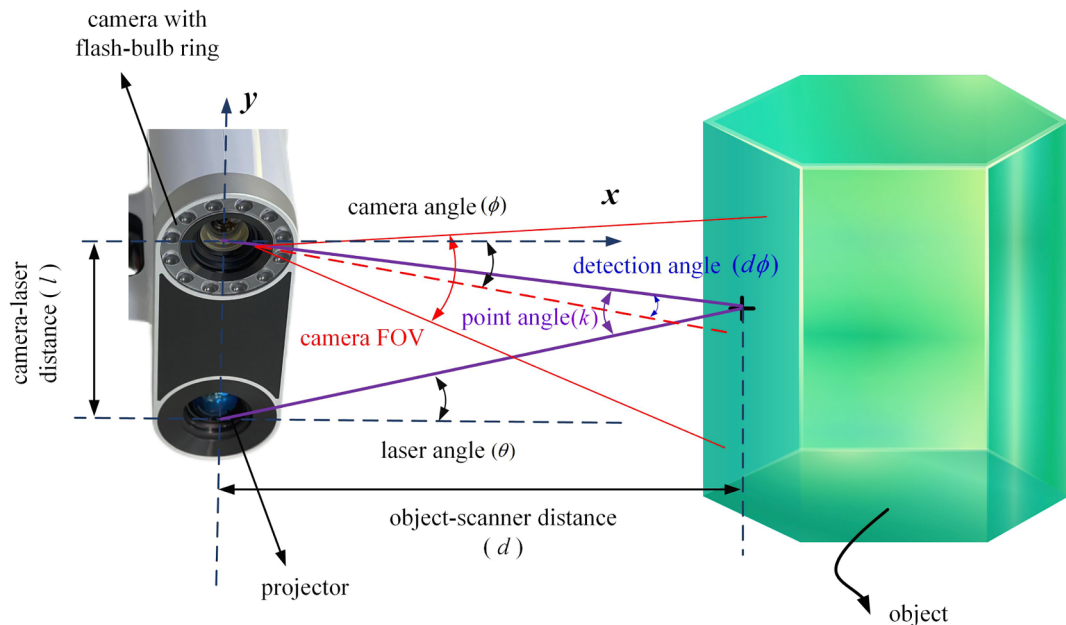


Fig. 8. Schematic diagram of the principle of structured light triangulation method.

computer to send and receive commands, modulating signals through an optical transceiver, converting them into optical signals, and transmitting them to the motor driver. The power supply for the motor is centrally controlled through a distribution cabinet. The accurate issuance of commands depends on the collection of various data inside the subsea dry cabin, including water level, attitude, images, illumination, tension, etc. Therefore, the operation of the SLSDS also requires

matching information with various sensors and actuators.

To enable remote control of the scanning process, an upper computer interface was designed as shown in Fig. 10. The upper computer interface is divided into several panels, among which those related to structured light scanning include the control panel responsible for switching the scanner's position within the dry cabin and the illumination and monitoring control panel. Other panels on the upper

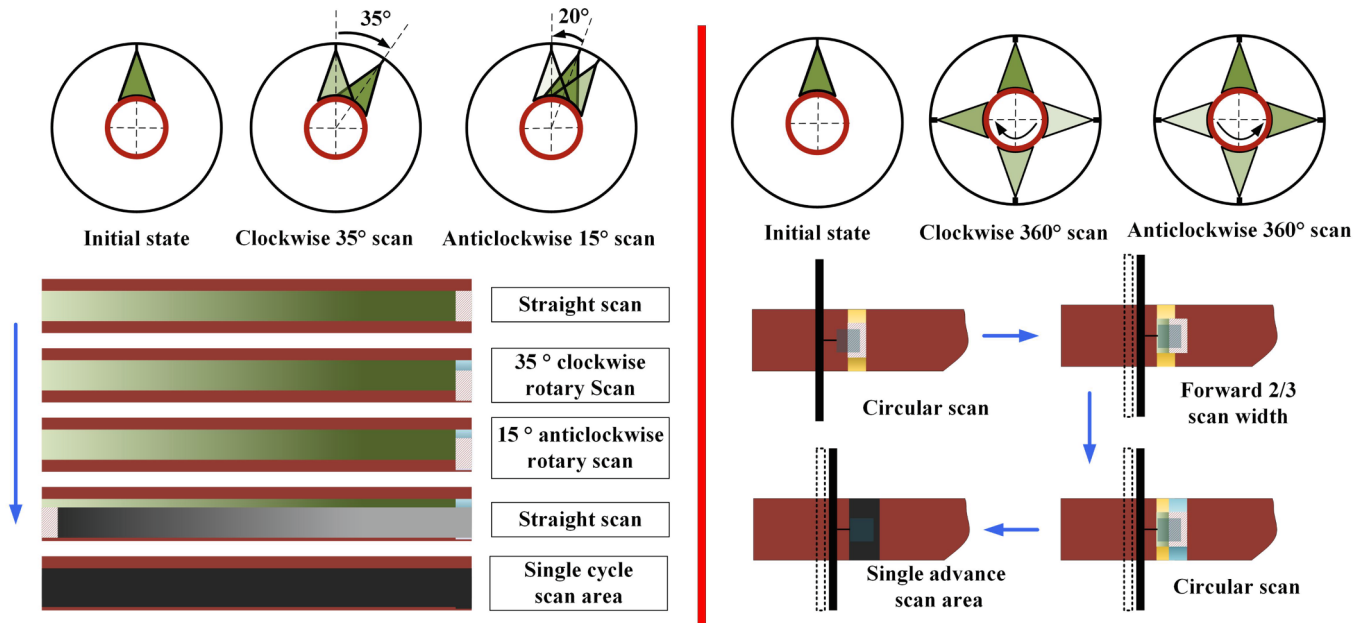


Fig. 9. Full coverage scanning strategy.



Fig. 10. Upper computer interface of the shipboard electrical control system.

computer interface include controls for hydraulic cylinders and hydraulic winches, as well as displays for attitude, water depth, temperature, module status, and running status. The interface information and subsea sensor data are transmitted and displayed in real-time, providing crucial references for pipeline scanning. By inputting the motor's rotation count on the interface, accurate axial movement distance, circumferential rotation angle, and scanner swing angle can be obtained through gear ratio conversion.

### 3. Experimental study

#### 3.1. Experimental setup

Sea trials are the optimal method to validate marine engineering equipment. As depicted in Fig. 11, in June 2022, our team conducted functional verification of the inspection device in the waters of Zhoushan City, Zhejiang Province, China. As the safety of the subsea pipelines requiring inspection and maintenance is of paramount importance, affecting the city's energy supply, this inspection device was deployed in advance on a steel structure platform, which was welded with experimental subsea pipeline, to simulate the real conditions and verify its functionality and safety. It is worth mentioning that the

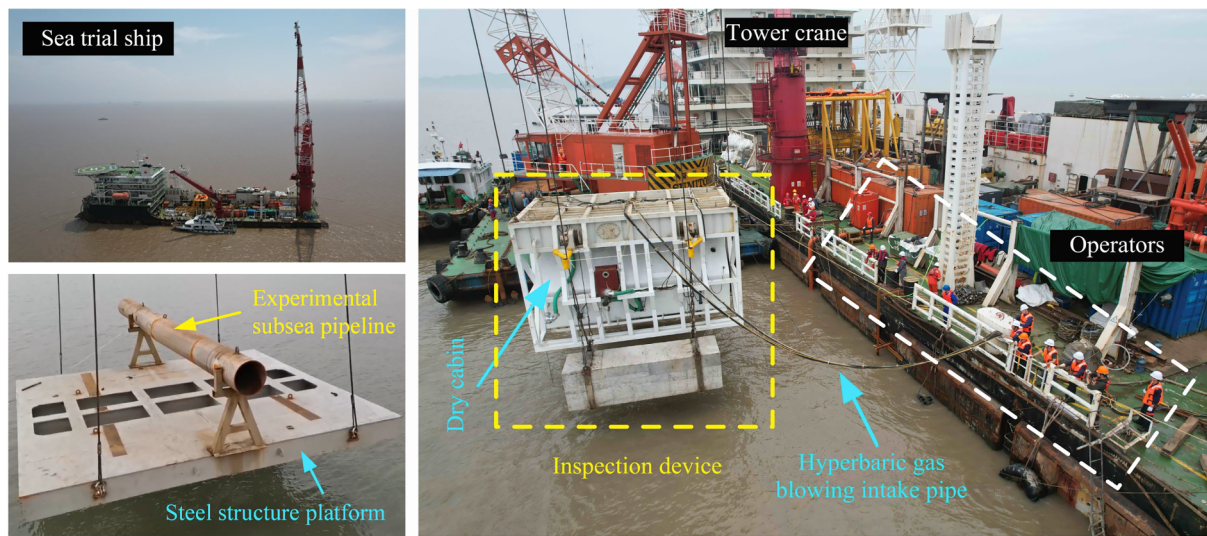


**Fig. 11.** Sea trial of the inspection device.

deformation dimensions of the subsea pipelines welded onto the steel structure platform are much larger than those found in actual subsea pipelines. However, all parameters, including external dimensions and material composition, resemble those of the defective subsea pipelines.

The experimental procedure involved first submerging a steel structure platform, welded with test subsea pipelines, near the actual subsea pipelines to ensure similarity to the seabed environment. Subsequently, the entire inspection device, along with the ballast weights, was lifted into the sea to facilitate cross-pipeline operations. The subsea dry cabin was then purged, followed by the surveying of subsea pipelines.

The relevant experimental parameters are presented in [Table 3](#). The experimental subsea pipeline was 12 m long, with a bending angle of 12°. The high-pressure purge gas was supplied at a pressure of 0.8 MPa, and the sea trial location had a water depth of 33 m. The vessel used for these sea trials was CPOE101, equipped with a tower crane with a lifting capacity of 200 tons, ensuring the smooth execution of the trial.

### 3.2. Hyperbaric gas blowing results

[Fig. 12](#) illustrates the monitoring of the medium displacement process in the subsea dry cabin. The liquid level within the cabin steadily decreases as pumps and high-pressure air are utilized (due to limitations in imaging conditions of the monitoring equipment, the initial fully submerged state is not visible). Consequently, the subsea pipelines start to become exposed to the air within the cabin.

[Fig. 13](#) illustrates a time-dependent chart depicting the rate of medium replacement and total volume of displaced liquid in the dry cabin over time. The evacuation speed exhibits non-constant behavior, initially peaking before gradually stabilizing at a lower rate. Subsequently, there is a notable surge in evacuation speed, ultimately returning to zero. Analysis of the underlying principles reveals that the

dry cabin's closed hexagonal structure, with its intake port positioned at the top, initially compresses high-pressure gas into a confined space, facilitating rapid drainage. However, as the cabin's air volume increases, the rise in gas pressure necessitates more time, resulting in a more gradual decline in the liquid level during the middle phase of evacuation. As the liquid level continues to decrease, the rate of volume change in the high-pressure gas slows down. Despite this, achieving liquid drainage still requires significant spatial displacement, thereby maintaining the evacuation speed at a relatively low level. During the sea trial, the activation of pumps (including submersible and pneumatic diaphragm pumps) expedites cabin drainage, notably enhancing evacuation speed during the final stage. Upon reaching the required water level for mapping purposes, the submersible pump is deactivated, leaving only the pneumatic diaphragm pump operational to sustain the water level. To ensure comprehensive protection of the dry cabin, high-pressure air is constantly supplied, despite the evacuation speed being zero at this point. The total drainage volume can be calculated by integrating the evacuation speed over time, as depicted by the trend in [Fig. 12](#) on the right.

### 3.3. Structured light mapping process

The calibration of SLS is the prerequisite for accurate data acquisition. The calibration for SLS scanning is performed according to the trajectory shown in [Fig. 14](#).

As shown in [Fig. 15](#), after the formation of the dry cabin, driving SLSDS's motors rotate to move the SLS inside the dry cabin, achieving the mapping of the experimental subsea pipelines. Due to the low light condition inside the dry cabin, which is unfavorable for structured light imaging of surface defects on the subsea pipelines, fill lights are used to improve lighting conditions inside the cabin. The fill lights installed outside the SLS chamber are waterproof and have a larger beam angle than the scanner's field of view (FOV), thereby ensuring the imaging quality of the scanner. To facilitate remote control, there are also 12 cameras installed inside the chamber to provide a comprehensive view of the chamber's interior. Moreover, to enhance the imaging conditions inside the dry cabin, eight additional fill lights are arranged (different from the fill lights of the SLS).

As described in [Fig. 8](#), the structured light mapping scheme consists of linear scanning and circular scanning. [Fig. 16](#) illustrates a single instance of circular scanning during the dry cabin mapping process.

The SLS is enclosed within the red box, and the red dashed line represents the connection between the scanner and the rotation center, indicating its position. After a clockwise 360-degree rotation of the

**Table 3**  
The applied forces, pressures, and dimensional parameters of safety verification.

Properties	Units	Values	Properties	Units	Values
Experimental subsea pipeline length	m	12	Experimental subsea pipeline bending angle	°	12
Hyperbaric gas pressure	MPa	0.8	The water depth at the sea trial location	m	33
Tower crane lifting capacity	T	200	Sea trial ship	/	CPOE101

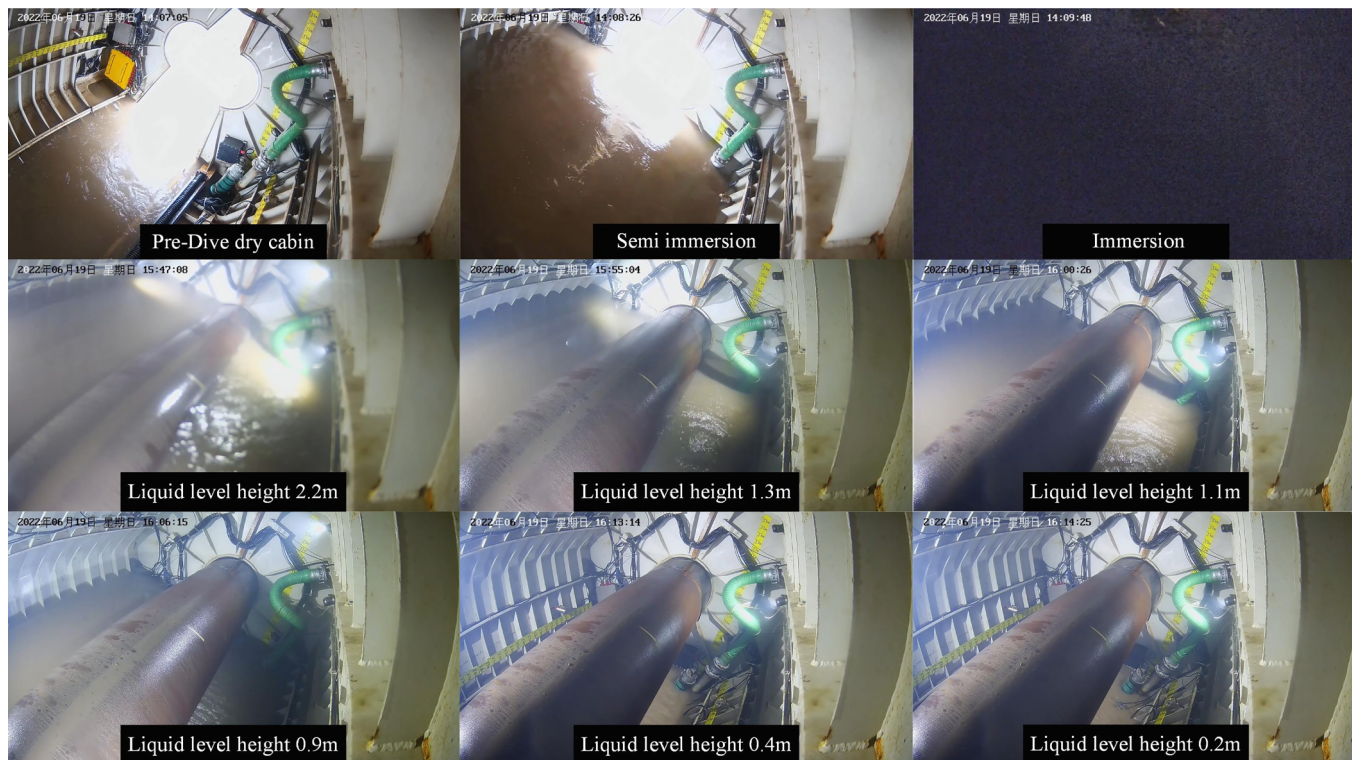


Fig. 12. Subsea dry cabin evacuation process monitoring.

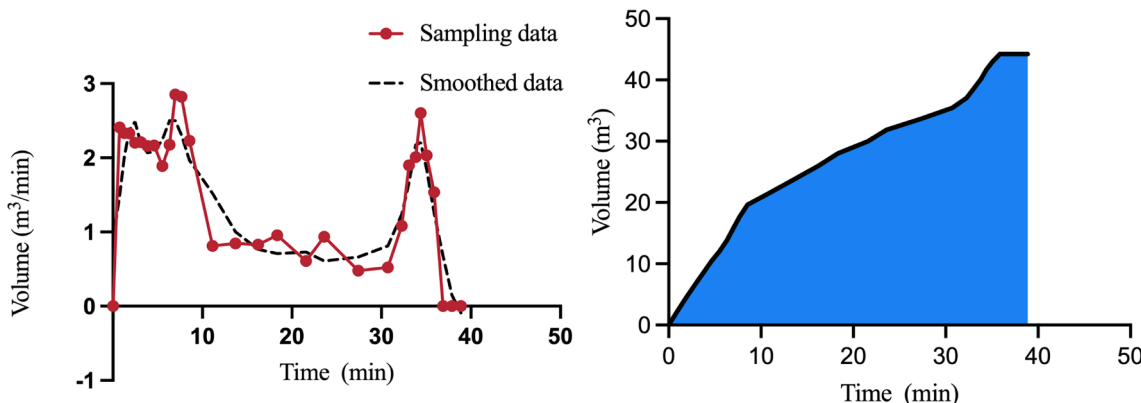


Fig. 13. Diagram of emptying rate versus time (left) and total drainage volume versus time (right).

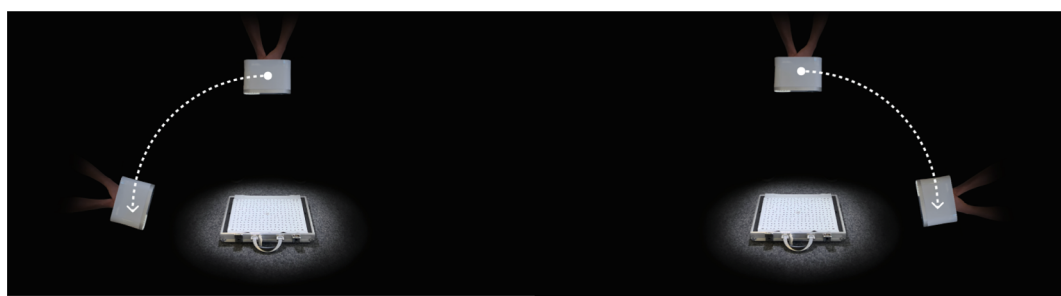


Fig. 14. Trajectories of scanning for recalibration [41].

scanner, the system moves forward and then proceeds with a counter-clockwise rotation of 360 degrees, completing a fundamental circular scanning motion. By repeating this process, a point cloud dataset of a segment of the subsea pipeline can be obtained.

However, due to the significant bends in the experimental subsea pipeline, it is not feasible to complete the scanning of all pipeline sections using a single circular scanning approach. Therefore, multiple mapping sessions are conducted, and each session does not strictly



Fig. 15. Structural light scanning physical image inside the dry cabin.

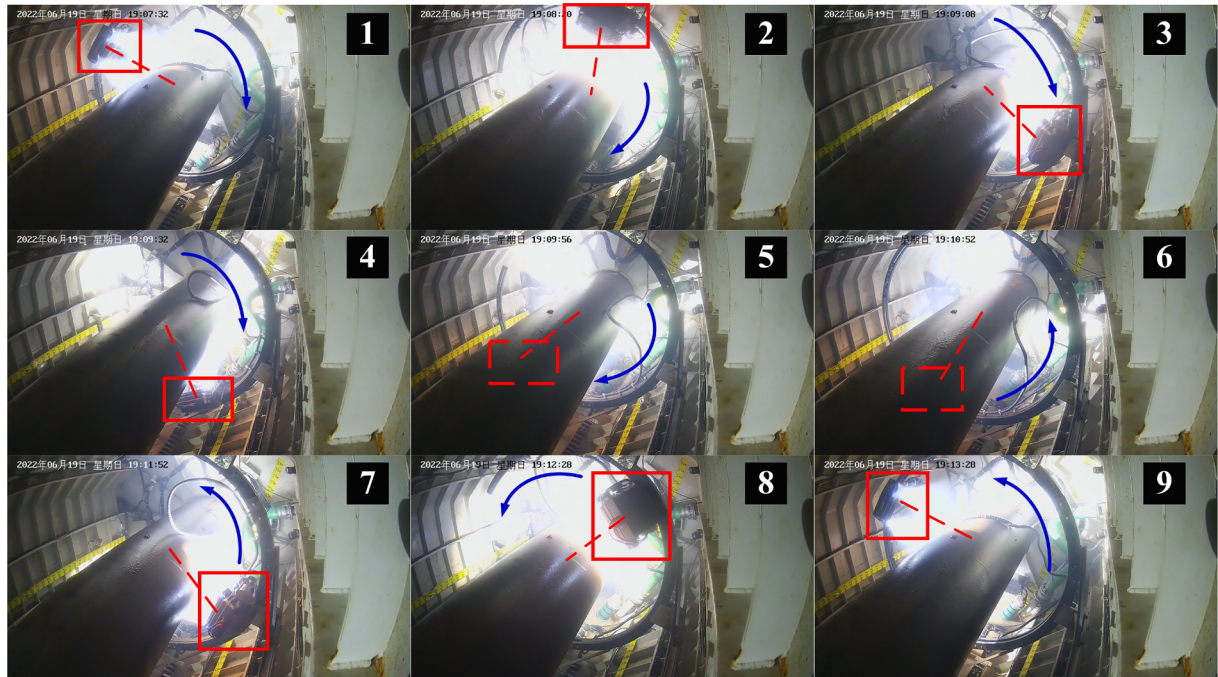


Fig. 16. A single instance of circular scanning.

adhere to either linear or circular scanning strategies. In cases where the quality of structured light scanning is insufficient, a flexible combination of scanning methods is employed to ensure data continuity and prevent interruptions in the mapping process (loss of scanned objects can lead to significant errors). When the perspective is not ideal, a combination of swiveling the scanner's angle, and linear or circular motion can be used to capture point cloud data continuously.

#### 3.4. Post-processing of point cloud data

After obtaining accurate surface data for the subsea pipeline, the first step is to apply filtering techniques to remove outliers, missing points, noise, and duplicate points. This study utilizes two methods for filtering: downsampling to remove redundancy and moving least squares (MLS).

The downsampling algorithm calculates the centroid  $V_0$  within the local neighborhood of the point cloud model. Other nearby points are weighted according to Equation (8), and the weighted centroid  $V_0$  is obtained through the weighted calculation within the local neighborhood.

$$V_0 = \frac{\sum_{j=1}^k \omega(V_0)p_{ij}}{\sum_{j=1}^k \omega(V_0)} \quad (12)$$

$$\omega(V_0) = \exp\left(-\frac{\|p_{ij} - V_0\|^2}{r^2}\right) \quad (13)$$

here,  $\omega(V_0)$  represents the Gaussian weighting function and  $r$  represents the neighborhood size. The larger the weight, the closer it is to the centroid  $V_0$ , and vice versa. Assuming the input point cloud is denoted as  $P$  and its corresponding global bounding surface is denoted as  $B$ , where  $l$ ,  $m$ , and  $n$  represent the number of subdivisions along the  $x$ ,  $y$ , and  $z$  axes, respectively,  $R_{ijk} = V_x \times V_y \times V_z$  represents the corresponding segmentation region for  $B$ , and  $i \in (0, l)$ ,  $j \in (0, m)$ ,  $k \in (0, n)$ , then we obtain the sampled output point cloud data  $P^*$ .

MLS is a method used to reconstruct continuous functions from a set of unorganized point samples. It involves calculating a weighted least squares measure that is biased towards the region surrounding the point at which the reconstructed value is required. Let  $P = \{p_i \in R^3\}$ ,  $i = \{1, 2,$

$3, \dots, n\}$  represent a point cloud set,  $S_{MLS}(P)$  denote its MLS surface, and  $\beta = \{X | d_{P(X)} < r_B\} = \bigcup B_i, B_i = \{X, \|X - p_i\| < r_B\}$  be a local neighborhood centered at  $P$ . The corresponding projection operation can be represented as  $\psi : \beta \rightarrow R^3$ . The MLS process can be described in three main steps for fitting a local surface  $g$  using a local reference surface  $H$ , for points in a point cloud.

First, we can compute the local reference plane  $H$  for  $r$  by evaluating a nonlinear energy function, which is defined as follows:

$$E_{MLS}(q, n) = \sum_i (n^T p_i - n^T q) \theta(\|p_i - q_i\|) \quad (14)$$

where  $n, q \in R^3, n = n(q) = (r - q)/\|(r - q)\|$ ,  $q$  represents the projection of  $r$  onto  $H$  and  $\theta$  denotes the Gaussian weight function, which is non-negative and monotonically decreasing.

Next, we compute the local polynomial approximation  $g$  of the surface near  $r$ , using weighted least squares fitting. We aim to minimize the error:

$$\sum_i (g(x_i, y_i) - f_i)^2 \theta(\|p_i - q_i\|) \quad (15)$$

Calculate the coefficients of  $g$  accordingly. Here,  $(x_i, y_i)$  represents the coordinates of  $q_i$ ,  $f_i$  represents the height of  $p_i$  with respect to the  $H$  plane. Finally, we obtain the projection of  $r: \psi(r) = q + g(0, 0) \cdot n$ .

As shown in Fig. 16, the input point cloud fragments have been processed using the aforementioned algorithm. However, fusing the two fragment combinations, namely Combination 1 and Combination 2, is difficult. Therefore, utilizing the align functionality of Artec Studio 16 Professional, markers are placed to create align pairs, yielding preliminary fusion results. Optimized these align pairs to obtain aligned point cloud data.

As a result of angle restrictions during the scanning process, certain sections of the surface data exhibit omissions, resulting in the emergence of voids. To mitigate this issue, Artec Studio's hole filling capability is engaged, effectively addressing the majority of the unoccupied areas. Nevertheless, some regions still suffer from inadequate overlapping.

Upon meticulous analysis, this predicament is attributed to potential alignment imprecisions and cumulative errors incurred during the scanning procedure, progressing from right to left. As a consequence, the cumulative error reaches its peak on the far-left side while diminishing towards the far-right side. To ameliorate this, further refinement techniques are applied, involving smoothing operations on the gathered data. The resulting output point cloud, as illustrated in Fig. 17, is attained through these enhancements.

Fig. 18 shows a comparison between the experimental pipeline and the output point cloud. The pipeline used in the sea trial is 12 m long, with a 6-meter section in the middle designated for inspection, and 3-meter straight sections at each end. The length of the pipeline represented in the output point cloud is 5.6 m, capturing the bend in the middle of the pipeline. Consequently, the pipeline appears relatively straight from the perspective of the sea trial, whereas the output point cloud appears more curved. This is a visual distortion, and we believe it is necessary to clarify this to avoid any misunderstanding.

The completion method for point cloud data in Artec Studio Professional 16 is not explicitly specified. As shown in Fig. 19, based on the network structure employed in point cloud completion and generation, the existing architectures could be categorized into point-based, view-based, convolution-based, graph-based, transformer-based, generative model-based, and other methods. Commonly used techniques for point cloud completion include Variational Autoencoder (VAE) and other deep learning algorithms such as the VRC-Net architecture. VAE is a generative model based on neural networks that can generate new data similar to the training data from a latent space. The core idea of VAE includes mapping the input data to a latent space (encoding process), randomly sampling from the latent space, and then mapping the sampled data back to the original data space (decoding process).

For 3D point cloud completion, the Chamfer Distance (CD) and Earth Mover's Distance (EMD) are the most frequently used performance criteria. CD tries to find the minimum distance between two sets of points, while EMD evaluates the reconstruction quality of the point clouds.

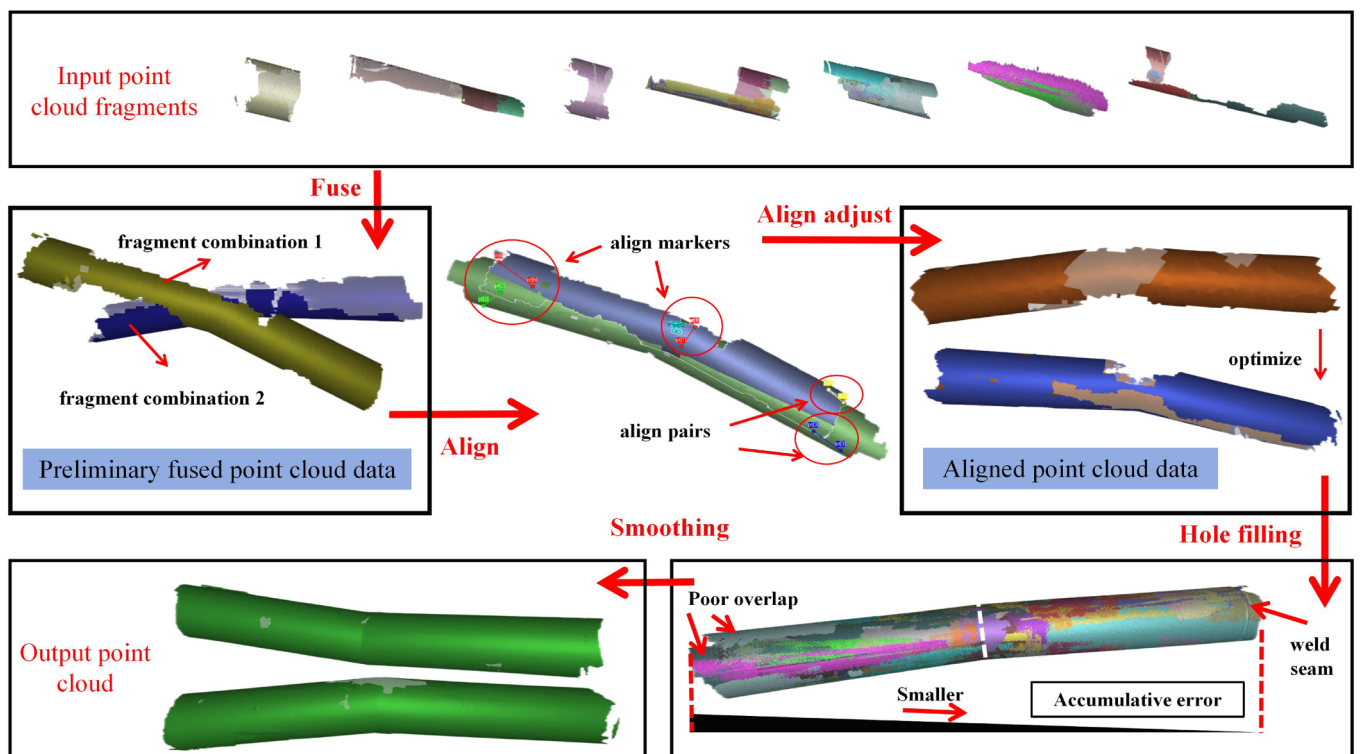
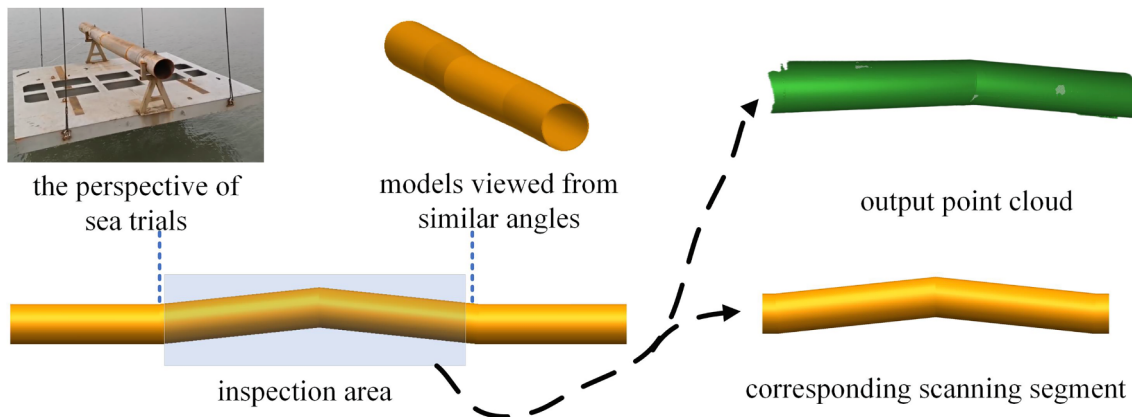
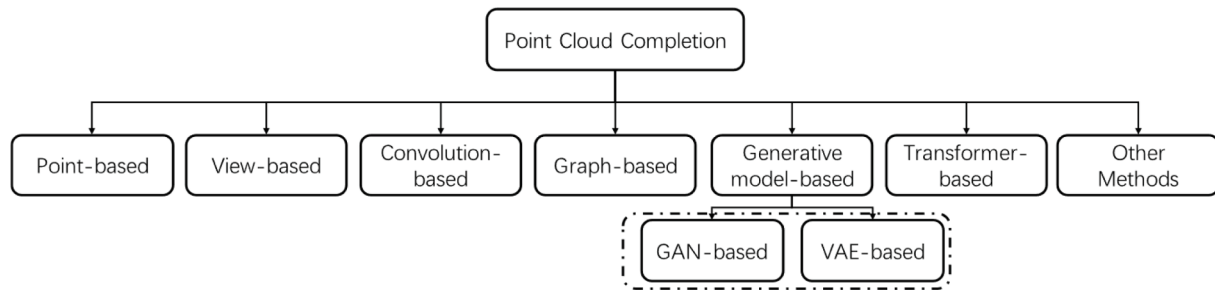


Fig. 17. Point cloud data post-processing flow chart.



**Fig. 18.** Comparison of the experimental pipeline and the output point cloud.



**Fig. 19.** Taxonomy of point cloud completion [42].

$$CD(\mathcal{S}_1, \mathcal{S}_2) = \frac{1}{|\mathcal{S}_1|} \sum_{x \in \mathcal{S}_1} \min_{y \in \mathcal{S}_2} \|x - y\|_2 + \frac{1}{|\mathcal{S}_2|} \sum_{y \in \mathcal{S}_2} \min_{x \in \mathcal{S}_1} \|y - x\|_2 \quad (16)$$

$$EMD(\mathcal{S}_1, \mathcal{S}_2) = \min_{\phi: \mathcal{S}_1 \rightarrow \mathcal{S}_2} \frac{1}{|\mathcal{S}_1|} \sum_{x \in \mathcal{S}_1} \|\phi(x) - x\|_2 \quad (17)$$

Other performance criteria include Density-Aware Chamfer Distance (DCD) and F-score. DCD is derived from CD and can detect disparities in density distributions. It pays attention to both the overall structure and local geometric details.

$$DCD(\mathcal{S}_1, \mathcal{S}_2) = \frac{1}{2} \left( \frac{1}{|\mathcal{S}_1|} \sum_{x \in \mathcal{S}_1} \left( 1 - \frac{1}{n_y} e^{-\alpha \|x - y\|_2} \right) + \left( \frac{1}{|\mathcal{S}_2|} \sum_{y \in \mathcal{S}_2} \left( 1 - \frac{1}{n_x} e^{-\alpha \|x - y\|_2} \right) \right) \right) \quad (18)$$

The F-score can evaluate the percentage of points or surface area that are reconstructed correctly, which can be defined as follows:

$$F-Score(d) = \frac{2P(d)R(d)}{P(d) + R(d)} \quad (19)$$

where  $P(d)$  and  $R(d)$  denote the precision and recall for a distance threshold  $d$ , respectively.

$$P(d) = \frac{1}{|\mathcal{S}_1|} \sum_{r \in \mathcal{S}_1} [\min_{t \in \mathcal{S}_2} \|t - r\| < d] \quad (20)$$

$$R(d) = \frac{1}{|\mathcal{S}_2|} \sum_{t \in \mathcal{S}_2} [\min_{r \in \mathcal{S}_1} \|t - r\| < d] \quad (21)$$

The resulting comprehensive 3D image, as illustrated in Fig. 16, faithfully portrays the true state of the tested subsea pipeline on the seafloor. The structured light photometry's high precision enabled local magnification and a clear display of surface features, such as the weld

seam. Consequently, inspecting the entire pipe section facilitated the identification of hazardous points for further analysis and treatment, enabling the assessment of pipe damage, deformation, bending, and corrosion degrees.

Structured light offers advantages in high-density data acquisition and extraction of multiple feature parameters unmatched by other techniques. The acquired data is quantifiable, editable, and can be interpolated, allowing extraction of bending angles at different distances along the pipeline and pipeline's axial lines, as depicted in Fig. 20 for the results of the subsea pipeline in this sea trial. Due to the structured light's extremely high accuracy, it achieves heights unattainable by conventional external inspection methods for pipeline defects. We determined the bending angle of the pipeline by detecting the angle between the cross-sections of the pipeline. Among a series of three-dimensional scanned and reconstructed cross-sections, we selected three pairs of symmetrical cross-sections near the end faces and two pairs of symmetrical cross-sections near the middle respectively for angle measurement. The detection results of the two pairs in the middle are  $12.0609^\circ$  and  $12.2065^\circ$  respectively (with errors  $< 2\%$ ), and the detection results of the three pairs near the end faces are  $11.4812^\circ$ ,  $11.4565^\circ$  and  $11.4903^\circ$  respectively (with errors  $< 5\%$ ).

To effectively assess and mitigate risks associated with subsea pipeline defects, a comprehensive digital approach is essential. This approach should integrate modeling uncertainty methods, propagation techniques, and metrics for measuring uncertainty. Advanced computational models are used to simulate potential pipeline defects and their impacts under various conditions. By incorporating uncertainty quantification methods, the digital system can accurately predict the likelihood and severity of defects, thus enhancing risk assessment. Propagation techniques, such as Monte Carlo Simulation, are employed to understand how uncertainties in input parameters influence overall risk predictions. A crucial task in this process is accurately describing the probability distribution to determine the best-fitted marginal distribution for the variables.

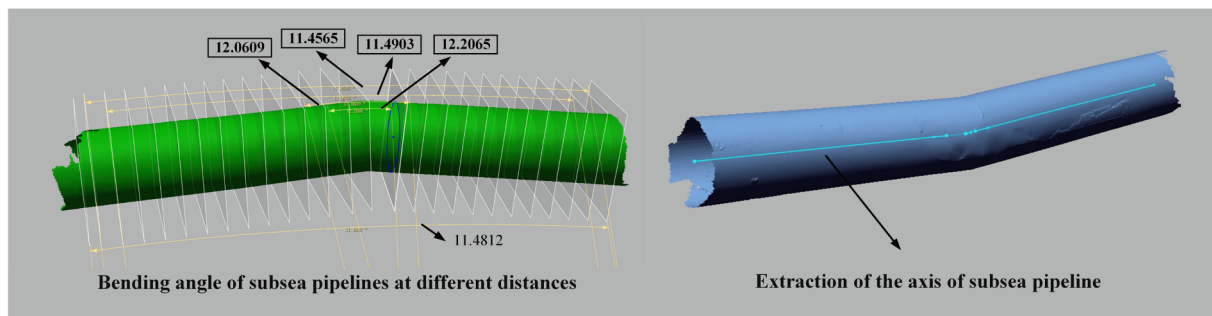


Fig. 20. Bending angle and axial line extraction diagram.

To seek simplicity, let us consider only the simple additive method here, which is described by a set of input variables  $X = (X_1, X_2, \dots, X_n)$  and one output variable  $Y$ . According to the Central Limit Theorem (CLT) and the Taylor series, the following formula can be derived [43]:

$$Y = g(\mu) + \sum_{i=1}^n \left[ \frac{\partial g(x)}{\partial X_i} \right]_{X=\mu} (X_i - \mu_i) + \frac{1}{2!} \sum_{i=1}^n \sum_{j=1}^n \left[ \frac{\partial^2 g(X)}{\partial X_i \partial X_j} \right]_{X=\mu} [(X_i - \mu_i)(X_j - \mu_j)] + \Delta \quad (22)$$

The term  $\Delta$  is a residual and includes the order of three and more. It should be highlighted that the derivatives are determined for the mean-nominal-value. Then the mean-nominal-value of  $Y$ :

$$E(Y) \approx g(\mu) + \frac{1}{2} \sum_{i=1}^n \left[ \frac{\partial^2 g(X)}{\partial X_i^2} \right]_{X=\mu} \sigma_i^2 \quad (23)$$

Then the variance of  $Y$ :

$$\text{Var}(Y) \approx \text{Var} \sum_{i=1}^n \left[ \frac{\partial g(x)}{\partial X_i} \right]_{X=\mu} (X_i - \mu_i) = \sum_{i=1}^n \left[ \frac{\partial g(x)}{\partial X_i} \right]_{X=\mu}^2 \sigma_i^2 \quad (24)$$

Metrics for measuring uncertainty help quantify the reliability of model predictions, providing a basis for decision-making in pipeline maintenance and management. This approach enhances understanding

of risks and supports the development of strategies to mitigate potential issues, ultimately improving pipeline safety and reliability.

#### 4. Discussion

The present study introduces an innovation in subsea pipeline inspection by proposing a novel approach to detect defects using a dry cabin and structured light technology. This method aims to enhance pipeline scanning by mitigating seawater interference and harnessing the precision of structured light technology. Furthermore, implementing dry cabin technology for subsea pipelines in China represents an advancement, albeit with uncertainties that must be addressed. Structured light technology, renowned for its high accuracy, finds widespread applications in various fields, such as reverse engineering, quality inspection, biometric identification, and medical modeling. However, its application in subsea pipeline defect inspection is unprecedented, rendering this study innovative. This approach holds promise for improving subsea pipeline inspection through non-destructive testing capable of identifying various defects, including cracks, dents, corrosion, and other damages.

As shown in Fig. 21, the Contacted Surface Profile Measuring Device (CSM), designed and manufactured by CPOE, was also utilized in the survey of external defects on the Cezhen subsea pipeline. The basic principle involves rotating around the pipeline while using a contact

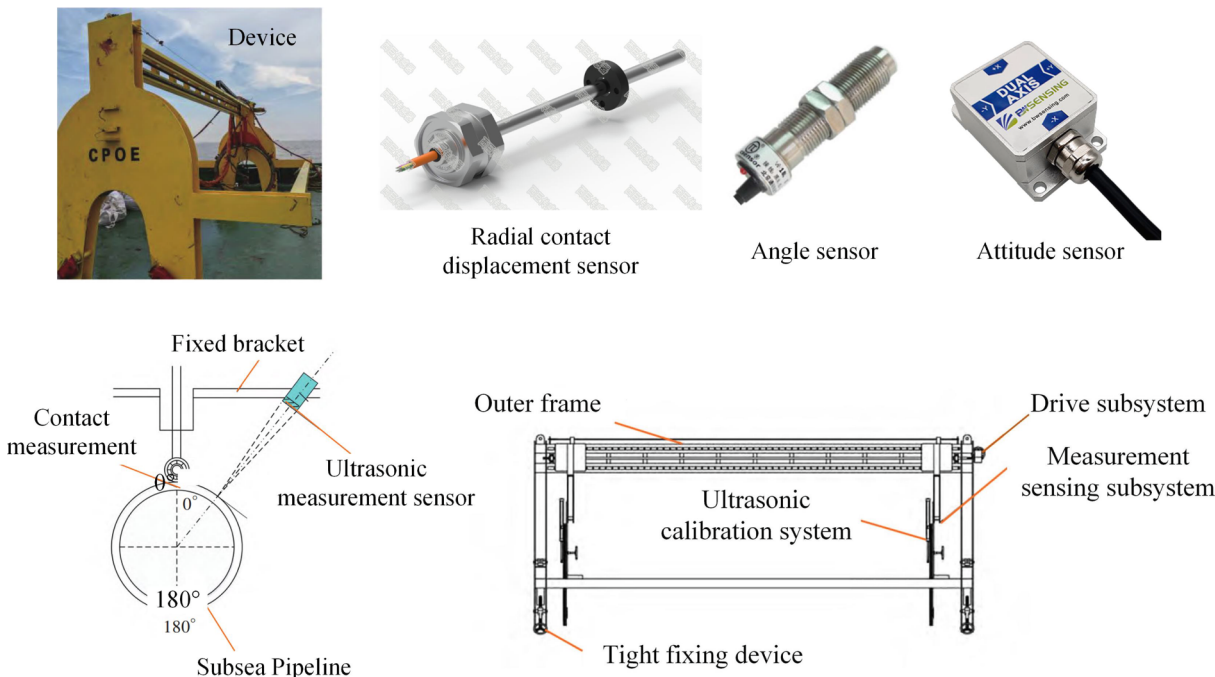


Fig. 21. Contacted surface profile measuring device [20].

displacement sensor to obtain radial deformation data, which is cross-verified with radial data from an ultrasonic sensor. By combining data from angular and attitude sensors, the device can assess the flatness and integrity of the pipeline surface.

Due to considerations of operational efficiency, the distance between adjacent circumferences during operation is not too small, as shown in Fig. 22, being approximately 100 mm. The circumferential sampling data points in CSM are limited by time constraints, and the number of sampling points is usually not set too high. In terms of the accuracy of the acquired surface deformation data, the structured light scanning device has a significant advantage over CSM. Moreover, because the entire surveying apparatus for contact point measurements is open-ended, it is susceptible to interference from ocean currents, marine life, and drifting objects, all of which can affect the surveying process. In contrast, structured light mapping operates within a closed environment, offering superior reliability.

It should be noted that since this method was used for the first time, a test pipeline section was chosen to avoid any potential safety threats to the actual operational pipeline. This test section was placed at the coordinate points of the target survey pipeline, and the survey was conducted accordingly, with all procedures strictly following the requirements for surveying a real pipeline. In contrast, the CSM, as a mature technology, was used to survey actual pipeline defect points. Therefore, the survey results shown in Fig. 23 are not from the same pipeline section, and some differences in the results are expected.

Although it is possible to achieve higher resolution by spending more time, the survey interval is typically not set too small. In contrast, the surface generated by structured light scanning is a smooth point cloud, with weld seams clearly visible upon magnification. According to the parameters of the structured light scanner, the point cloud accuracy is  $0.1 \text{ mm} + 0.3 \text{ mm/m}$ , with the maximum survey area of this device being approximately 1.1 m, resulting in a minimum accuracy of 0.43 mm. Of course, this is only the theoretical scanning accuracy of the scanning device. Affected by factors such as the actual environment and the driving mechanism, the actual scanning accuracy will decrease to some extent. However, as indicated in Fig. 23, through scanning experiments, we detected a pipeline scratch with an actual width of about 1.6 mm, which proves the accuracy advantage of the structured light scanning device.

Structured light scanning can be completed within six hours, and considering the semidiurnal tides in the Zhoushan Sea area, which allow for deployment and retrieval only during slack tide periods, a single day suffices for surveying one location. This represents a substantial

efficiency gain of 50–66.7 % compared to traditional methods such as the CSM. The high operational costs of large pipelay vessels, driven by expenses related to personnel, equipment, and fuel, make time a critical factor. Our method significantly reduces these costs by decreasing the time required for external pipeline defect surveys. Furthermore, the defect assessment derived from structured light scanning provides more accurate and reliable data, essential for long-term maintenance strategies. Timely and precise repairs not only prevent costly environmental remediation and emergency interventions associated with leaks but also contribute to sustainable pipeline management. The accumulation of insights from successive repairs fosters the development of more effective and efficient maintenance strategies, enhancing repair quality and extending the pipeline's operational lifespan. This approach promises significant cost savings and improved environmental stewardship over the pipeline's lifecycle.

Despite its potential benefits, the current project requires further refinement, particularly in the sealing structure of the dry cabin. Redesigning is imperative to minimize leaks and preserve the integrity of the high-pressure drainage effect. The existing sealing structure's limitations may compromise the dry environment and diminish the effectiveness of the pipeline scanning process. Exploring superior sealing methods or materials could enhance adaptability to larger pipeline defects.

Moreover, the driving structure for the structured light survey exhibits certain structural deficiencies, leading to operational issues such as poor performance and inadequate motor energy. Addressing these shortcomings is crucial to enhance the overall efficiency of the scanning process. Future studies should explore alternative driving structures and hydraulic driving methods to improve energy density and implement advanced motor control systems for real-time speed regulation and power distribution.

Furthermore, the reliance on manual input for the SLDS operation introduces inconvenience. To mitigate this limitation, leveraging real-time data quality discrimination to automate motor rotation through algorithmic means is proposed. This would facilitate automated scanning of subsea pipelines, thereby reducing potential hazards associated with human error. Enhancements in lighting, control programs, and other relevant aspects should be considered in future iterations.

In light of the rapid advancements in artificial intelligence, AI can be harnessed to conduct image recognition using multiple cameras within the chamber, allowing for real-time monitoring of the scanning process and automation of command transmission. This capability not only streamlines operations but also enhances precision and responsiveness.

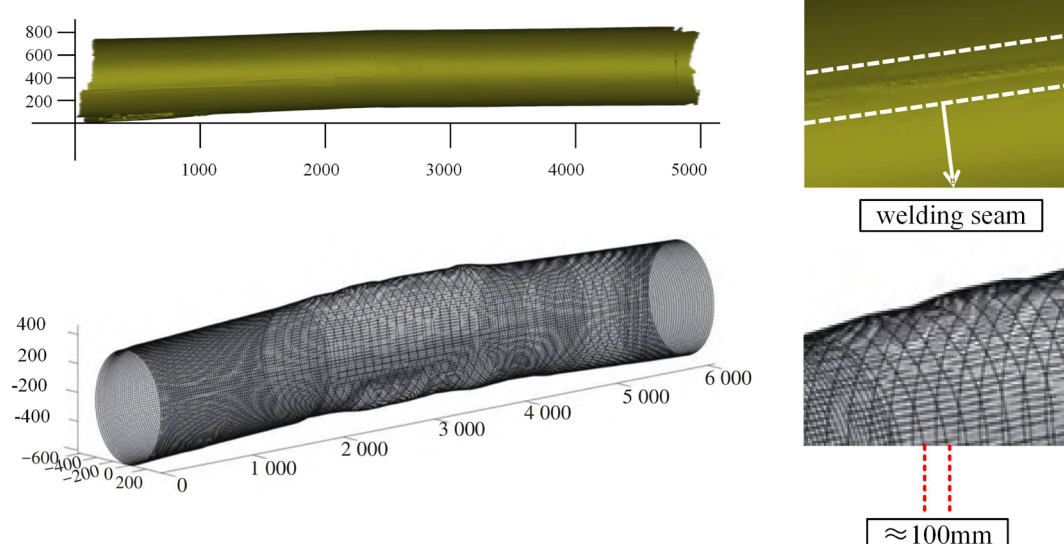


**Fig. 22.** Comparison of external mapping results between two methods [20].

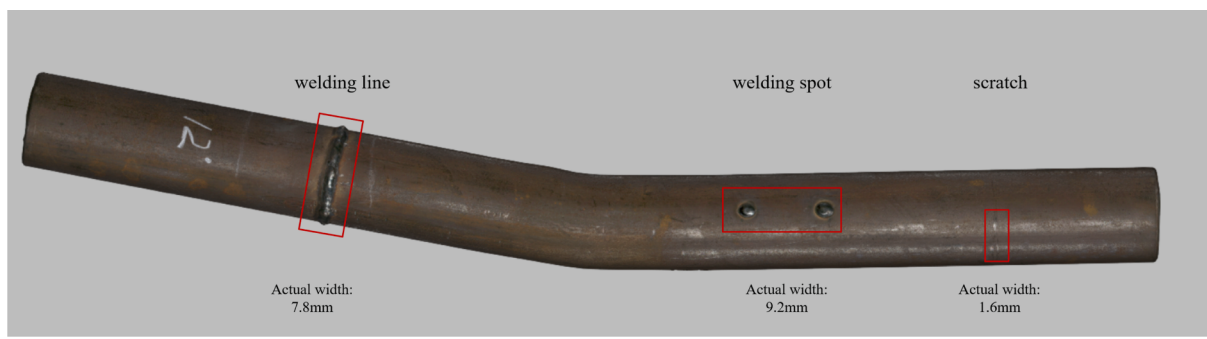


**Fig. 23.** Results of Structured Light Scanning for Small Pipeline Defects.

AI can leverage big data analysis of images to perform a comprehensive comparison and validation of results against those obtained through structured light mapping. This integration provides a robust framework for defect assessment, enabling a more nuanced understanding of discrepancies and potential issues. In the context of extreme marine environments, such as operations at very deep seabeds, unmanned operations become not only viable but essential. The deployment of AI and other cutting-edge technologies like big data analytics offers a transformative approach to underwater surveying, ensuring high efficiency while minimizing risks. These advancements pave the way for safer, more reliable pipeline inspections in challenging conditions.

The device is highly adaptable to different operating depths. By providing high-pressure air at various pressures, it can accommodate different water depths. The only limitation is the human endurance threshold under high-pressure conditions. Saturation diving could be considered for deeper operations, with records indicating that a depth of 300 m may be the maximum that can be attempted. In the more distant future, technical advancements could enable unmanned remote surveying, overcoming depth limitations while mitigating safety risks.

For pipelines of different diameters, the device is downwardly compatible, meaning it can be used for pipelines with diameters of less than 762 mm and bends of less than 15°. The only additional work required is a redesign of the seal between the pipeline and the chamber to match the chamber opening radius with the specific pipeline size. In the future, quick-change interfaces for commonly used pipeline sizes could be considered at the seal to enhance adaptability.

No equipment can guarantee absolute safety, and subsea pipeline operations inherently carry potential risks that could impact the marine environment. While we conducted safety validations in Section 2.2, it is crucial to acknowledge the environmental challenges that equipment might pose. For example, hydraulic systems could potentially leak oil, operational activities might disrupt the seabed ecology, and the paint used for equipment coatings could be harmful to marine life due to its toxic properties.

Addressing these environmental concerns requires a proactive approach. Although some of these hazards may be difficult to eliminate entirely in the foreseeable future, efforts should focus on innovative design solutions that prioritize safety and environmental stewardship. This includes developing safer structural designs and using eco-friendly materials and coatings. By advancing these areas, we can mitigate risks and contribute to more sustainable marine operations.

Additionally, incorporating repair functions is essential for comprehensive subsea pipeline inspection and maintenance. Potential repair methods include welding, clamps, external wrapping with composite patches, and algorithm-driven adaptive structured light surveys. By integrating these functions, an efficient system can be developed for detecting, diagnosing, and repairing pipeline defects.

In subsequent stages, research will focus on developing an integrated system for unmanned pipeline scanning and repair based on dry cabin technology. This will involve exploring key technologies such as flexible

leak-proof sealing, precise medium replacement, automated pipeline scanning, and unmanned repair. Modular detection and repair tools based on dry cabins will be developed, paving the way for manned solutions for subsea pipeline repair to ensure safe and stable operation.

Asset integrity failures can be minimized by implementing the digitized corrosion models and risk-based inspection methods associated with the objective.

## 5. Summary

In conclusion, this paper introduces a novel approach for subsea pipeline defect mapping utilizing the subsea dry cabin and structured light scanning technology. The subsea dry cabin is established by expelling seawater from the subsea cabin using high-pressure gas in conjunction with submersible and diaphragm pumps, allowing for rapid scanning implementation within a short timeframe during slack-water conditions. Additionally, scanning strategies are devised within the constraints of the limited scanning radius and SLS capabilities to ensure comprehensive coverage of the subsea pipeline surface.

The successful application of the subsea dry cabin for scanning expandable subsea pipelines in China represents an achievement, addressing numerous challenges associated with traditional subsea pipeline scanning techniques, such as measurement errors due to water flow, impurity interference, contact damage, and positioning difficulties. Furthermore, using structured light 3D scanning technology overcomes limitations inherent in other non-destructive testing (NDT) techniques, including restricted data information, small data samples, diminished accuracy, and high processing thresholds. The high precision, data editability, and versatile forms of structured light scanning data processing establish a robust foundation for its application in subsea pipeline defect scanning. Future research endeavors may extend the application of the subsea dry cabin and structured light scanning technology to diverse domains, encompassing ship hull inspection, pile foundation examination for offshore platforms, and offshore wind farm maintenance.

In summary, the amalgamation of the subsea dry cabin and structured light scanning technology presents a promising avenue for subsea pipeline defect inspection. This study showcases the feasibility and effectiveness of this approach while providing valuable insights into its application. This innovative methodology holds the potential to significantly enhance the accuracy, efficiency, and safety of subsea pipeline scanning, thereby contributing substantially to the maintenance and management of offshore infrastructure.

## CRediT authorship contribution statement

**Hai Zhu:** Writing – original draft, Methodology, Conceptualization.  
**Yuan Lin:** Writing – review & editing. **Zhangyong Jin:** Writing – original draft. **Jin Guo:** Writing – review & editing. **Peiwen Lin:** Validation, Software, Investigation. **Jiawang Chen:** Writing – review & editing, Supervision, Project administration, Methodology, Funding

acquisition, Conceptualization. **Jie Chen:** Validation, Supervision, Investigation. **Han Ge:** Writing – review & editing. **Kaichuang Wang:** Validation, Investigation. **Haonan Li:** Validation, Investigation. **Xiaoqing Peng:** Validation, Software, Investigation. **Peng Zhou:** Validation, Software, Investigation. **Yuping Fang:** Validation, Investigation. **Xueyu Ren:** Validation, Investigation, Conceptualization. **Yuhong Wang:** Validation, Investigation. **Yongqiang Ge:** Writing – review & editing. **Xu Gao:** Validation, Supervision, Investigation. **Yuanjie Chen:** Validation, Supervision, Investigation.

## Declaration of competing interest

The authors declare the following financial interests/personal relationships which may be considered as potential competing interests: [Jiawang Chen reports financial support was provided by Pipe China Eastern Oil Storage and Transportation Co. Ltd. Jiawang Chen reports financial support was provided by the Eyas Program Incubation Project of Zhejiang Provincial Administration for Market Regulation].

## Acknowledgments

We would like to express our sincere gratitude to the engineers and graduate students from the research group of Professor Jiawang Chen at the School of Oceanography, Zhejiang University, for their dedicated efforts in this study. We are also grateful for the financial support provided by Donghai Laboratory, PipeChina Eastern Oil Storage and Transportation Co., Ltd., and Zhejiang Institute of Metrology. Our work was also supported by the Key Research and Development Program of Zhejiang Province (No. 2024SSYS0089). Furthermore, we acknowledge the platform support from Zhejiang University, China.

## Data availability

Data will be made available on request.

## References

- [1] C. Schofield, Oceans: the blue frontier, *Nature* 469 (2011) 158–159, <https://doi.org/10.1038/469158a>.
- [2] Z. Hai, C. Jia-wang, R. Zi-qiang, Z. Pei-hao, G. Qiao-ling, L. Xiao-ling, X. Chun-ying, H. Kai, Z. Peng, G. Feng, F. Yu-ping, A new technique for high-fidelity cutting technology for hydrate samples, *J. Zhejiang Univ.-Sci. A* 23 (2022) 40–54, <https://doi.org/10.1631/jzus.A2100188>.
- [3] B. Zhang, R. Gong, T. Wang, Z. Wang, Causes and treatment measures of submarine pipeline free-spanning, *J. Mar. Sci. Eng.* 8 (2020) 329, <https://doi.org/10.3390/jmse8050329>.
- [4] J. Chu, Y. Liu, X. Lv, Q. Li, H. Dong, Y. Song, J. Zhao, Experimental investigation on blockage predictions in gas pipelines using the pressure pulse wave method, *Energy* 230 (2021) 120897, <https://doi.org/10.1016/j.energy.2021.120897>.
- [5] Bai Y., Bai Q., eds., *Ocean Engineering Series*, in: *Subsea Pipelines Risers*, Elsevier Science Ltd, Oxford, 2005: p. ii. DOI: 10.1016/B978-008044566-3.50045-2.
- [6] X. Guo, T. Nian, F. Wang, L. Zheng, Landslides impact reduction effect by using honeycomb-hole submarine pipeline, *Ocean Eng.* 187 (2019) 106155, <https://doi.org/10.1016/j.oceaneng.2019.106155>.
- [7] K.Y. Lam, Z. Zong, Q.X. Wang, Dynamic response of a laminated pipeline on the seabed subjected to underwater shock, *Compos. Part B Eng.* 34 (2003) 59–66, [https://doi.org/10.1016/S1359-8368\(02\)00072-0](https://doi.org/10.1016/S1359-8368(02)00072-0).
- [8] M. Meriem-Benziane, S.A. Abdul-Wahab, H. Zahloul, B. Babaziane, M. Hadj-Meliani, G. Pluvinage, Finite element analysis of the integrity of an API X65 pipeline with a longitudinal crack repaired with single- and double-bonded composites, *Compos. Part B Eng.* 77 (2015) 431–439, <https://doi.org/10.1016/j.compositesb.2015.03.008>.
- [9] X. Hu, C. Zhou, M. Duan, C. An, Reliability analysis of marine risers with narrow and long corrosion defects under combined loads, *Pet. Sci.* 11 (2014) 139–146, <https://doi.org/10.1007/s12182-014-0325-6>.
- [10] A. Khan, S.S.A. Ali, A. Anwer, S.H. Adil, F. Mériaudeau, Subsea pipeline corrosion estimation by restoring and enhancing degraded underwater images, *IEEE Access* 6 (2018) 40585–40601, <https://doi.org/10.1109/ACCESS.2018.2855725>.
- [11] M.E.A. Ben Seghier, Z. Mustaffa, T. Zayed, Reliability assessment of subsea pipelines under the effect of spanning load and corrosion degradation, *J. Nat. Gas Sci. Eng.* 102 (2022) 104569, <https://doi.org/10.1016/j.jngse.2022.104569>.
- [12] Y.-M. Shi, N. Wang, F.-P. Gao, W.-G. Qi, J.-Q. Wang, Physical modeling of the axial pipe-soil interaction for pipeline walking on a sloping sandy seabed, *Ocean Eng.* 178 (2019) 20–30, <https://doi.org/10.1016/j.oceaneng.2019.02.059>.
- [13] Y. Li, J. Shuai, Z.-L. Jin, Y.-T. Zhao, K. Xu, Local buckling failure analysis of high-strength pipelines, *Pet. Sci.* 14 (2017) 549–559, <https://doi.org/10.1007/s12182-017-0172-3>.
- [14] H. Ji, W. Liu, K. Yang, J. Jiang, Z. Xing, Y. Wang, S. Zhao, Physical model experiment on the influence of water depth on the underwater pipeline surface impacted by landslide surge, *Sci. Rep.* 11 (2021) 19301, <https://doi.org/10.1038/s41598-021-98324-x>.
- [15] M. Jia, F. Li, Y. Zhang, M. Wu, Y. Li, S. Feng, H. Wang, H. Chen, W. Ju, J. Lin, J. Cai, Y. Zhang, F. Jiang, The Nord Stream pipeline gas leaks released approximately 220,000 tonnes of methane into the atmosphere, *Environ. Sci. Ecotechnology* 12 (2022) 100210, <https://doi.org/10.1016/j.ee.2022.100210>.
- [16] H. Zhu, J. Chen, Y. Lin, J. Guo, X. Gao, Y. Chen, Y. Ge, W. Wang, In-Line Inspection (ILI) techniques for subsea pipelines: state-of-the-art, *J. Mar. Sci. Eng.* 12 (2024) 417, <https://doi.org/10.3390/jmse12030417>.
- [17] W. Chen, Z. Liu, H. Zhang, M. Chen, Y. Zhang, A submarine pipeline segmentation method for noisy forward-looking sonar images using global information and coarse segmentation, *Appl. Ocean Res.* 112 (2021) 102691, <https://doi.org/10.1016/j.apor.2021.102691>.
- [18] M. Guan, Y. Cheng, Q. Li, C. Wang, X. Fang, J. Yu, An effective method for submarine buried pipeline detection via multi-sensor data fusion, *IEEE Access* 7 (2019) 125300–125309, <https://doi.org/10.1109/ACCESS.2019.2938264>.
- [19] Y. Zhang, H. Zhang, J. Liu, S. Zhang, Z. Liu, E. Lyu, W. Chen, Submarine pipeline tracking technology based on AUVs with forward looking sonar, *Appl. Ocean Res.* 122 (2022) 103128, <https://doi.org/10.1016/j.apor.2022.103128>.
- [20] L. Wang, G. Cao, Y. Ding, T. Zhang, K. Wang, Construction application of precise measurement technology on deformation of submarine pipelines based on pipeline clamp repair scheme, *Pet. Eng. Constr.* 49 (2023) 8–12.
- [21] H. Ravanbod, Application of neuro-fuzzy techniques in oil pipeline ultrasonic nondestructive testing, *NDT E Int.* 38 (2005) 643–653, <https://doi.org/10.1016/j.ndteint.2005.03.001>.
- [22] S. She, Y. Chen, Y. He, Z. Zhou, X. Zou, Optimal design of remote field eddy current testing probe for ferromagnetic pipeline inspection, *Measurement* 168 (2021), <https://doi.org/10.1016/j.measurement.2020.108306>.
- [23] Peng X., Anyaoha U., Liu Z., Tsukada K., Analysis of Magnetic-Flux Leakage (MFL) Data for Pipeline Corrosion Assessment, *IEEE Trans. Magn.* 56 (2020) 1–15. DOI: Design Issues and Challenges of Long-Range Ultrasonic.
- [24] J. Wang, R. He, H. Zhang, H. Guo, Q. Wu, State-of-the-art advancement and development direction of submarine pipeline inspection technology, *China Pet. Mach.* 44 (2016) 112–118, <https://doi.org/10.16082/j.cnki.issn.1001-4578.2016.10.025>.
- [25] S. Zhang, High-speed 3D shape measurement with structured light methods: a review, *Opt. Lasers Eng.* 106 (2018) 119–131, <https://doi.org/10.1016/j.optlaseng.2018.02.017>.
- [26] J. Geng, Structured-light 3D surface imaging: a tutorial, *Adv. Opt. Photonics* 3 (2011) 128–160, <https://doi.org/10.1364/AOP.3.000128>.
- [27] J.H.T. Daemen, T.G.J. Loonen, A.C. Verhulst, T.J.J. Maal, J.G. Maessen, Y.L. J. Vissers, K.W.E. Hulsewé, E.R. de Loos, Three-dimensional imaging of the chest wall: a comparison between three different imaging systems, *J. Surg. Res.* 259 (2021) 332–341, <https://doi.org/10.1016/j.jss.2020.09.027>.
- [28] Z. Wu, W. Guo, Q. Zhang, H. Wang, X. Li, Z. Chen, Time-overlapping structured-light projection: high performance on 3D shape measurement for complex dynamic scenes, *Opt. Express* 30 (2022) 22467–22486, <https://doi.org/10.1364/OE.460088>.
- [29] J. Ye, C. Zhou, Time-resolved coded structured light for 3D measurement, *Microw. Opt. Technol. Lett.* 63 (2021) 5–12, <https://doi.org/10.1002/mop.32548>.
- [30] Z. Zhuo, C. Zhu, C.-S. Tang, H. Xu, X. Shi, V. Mark, 3D characterization of desiccation cracking in clayey soils using a structured light scanner, *Eng. Geol.* 299 (2022) 106566, <https://doi.org/10.1016/j.enggeo.2022.106566>.
- [31] H. Cui, W. Liao, N. Dai, X. Cheng, A flexible and rapid micro-adjustment algorithm for structured light 3D measurement system with camera-projector, *Optik* 123 (2012) 109–116, <https://doi.org/10.1016/j.jleco.2011.03.008>.
- [32] K. Zhang, P. Chermayrong, F. Xiao, D. Tzoumanikas, B. Dams, S. Kay, B.B. Kocer, A. Burns, L. Orr, C. Choi, D.D. Darekar, W. Li, S. Hirschmann, V. Soana, S.A. Ngah, S. Sareh, A. Choubey, L. Margheri, V.M. Pawar, R.J. Ball, C. Williams, P. Shepherd, S. Leutenegger, R. Stuart-Smith, M. Kovac, Aerial additive manufacturing with multiple autonomous robots, *Nature* 609 (2022) 709–717, <https://doi.org/10.1038/s41586-022-04988-4>.
- [33] P.A.N. Yueran, Y.A.N.G. Baofeng, Design of sealing door of dry work chamber with normal pressure applied in subsea pipeline repair, *Pet. Eng. Constr.* 42 (2016) 46–49.
- [34] M. Berge, L. Birdsall, A. Erickson, T. Vernon, Underwater Habitat Clamp (UHC): an innovative partnership in underwater pipeline repair, *Am. Soc. Mechanical Engineers Digital Collect.* (2009) 193–200, <https://doi.org/10.1115/IPC2008-64607>.
- [35] C. Carlsen, T. Nagdhana, The nautilus robotic solution: a single robot that integrates inspection + maintenance + repair capabilities for subsea Pipelines and Tubulars, *OnePetro* (2024), <https://doi.org/10.4043/34668-MS>.
- [36] Y. Tong, Y. Cai, A. Nevin, Q. Ma, Digital technology virtual restoration of the colours and textures of polychrome Bodhidharma statue from the Lingyan Temple, Shandong, China, *Herit. Sci.* 11 (2023) 12, <https://doi.org/10.1186/s40494-023-00858-y>.
- [37] L. Li, N. Schemenauer, X. Peng, Y. Zeng, P. Gu, A reverse engineering system for rapid manufacturing of complex objects, *Robot. Comput.-Integr. Manuf.* 18 (2002) 53–67, [https://doi.org/10.1016/S0736-5845\(01\)00026-6](https://doi.org/10.1016/S0736-5845(01)00026-6).

- [38] X. Zexiao, W. Jianguo, Z. Qiumei, Complete 3D measurement in reverse engineering using a multi-probe system, *Int. J. Mach. Tools Manuf.* 45 (2005) 1474–1486, <https://doi.org/10.1016/j.ijmachtools.2005.01.028>.
- [39] L. Song, X. Li, Y. Yang, X. Zhu, Q. Guo, H. Liu, Structured-light based 3D reconstruction system for cultural relic packaging, *Sensors* 18 (2018) 2981, <https://doi.org/10.3390/s18092981>.
- [40] K. Wang, J. Chen, J. Huang, P. Lin, J. Guo, H. Zhu, Y. Fang, X. Chen, G. Cao, W. Jia, X. Gao, H. Ge, Investigation of dry environment construction Equipment's medium displacement system for submarine pipelines, *Ocean Eng.* 300 (2024) 117365, <https://doi.org/10.1016/j.oceaneng.2024.117365>.
- [41] Calibration — Artec Leo documentation, (n.d.). [https://docs.artec-group.com/leo\\_1.6/calibration.html](https://docs.artec-group.com/leo_1.6/calibration.html) (accessed April 29, 2024).
- [42] B. Fei, W. Yang, W.-M. Chen, Z. Li, Y. Li, T. Ma, X. Hu, L. Ma, Comprehensive review of deep learning-based 3D point cloud completion processing and analysis, *IEEE Trans. Intell. Transp. Syst.* 23 (2022) 22862–22883, <https://doi.org/10.1109/TITS.2022.3195555>.
- [43] M. Yazdi, E. Zarei, S. Adumene, R. Abbassi, P. Rahnamayezekavat, Chapter Eleven - Uncertainty modeling in risk assessment of digitalized process systems, in: F. Khan, H. Pasman, M. Yang (Eds.), *Methods Chem. Process Saf.*, Elsevier, 2022: pp. 389–416. DOI: 10.1016/bs.mcps.2022.04.005.